

# **1 Automated seismic waveform location using Multichannel**

## **2 Coherency Migration (MCM)–I. Theory**

**3** Peidong Shi,<sup>1\*</sup> Doug Angus,<sup>2</sup> Sebastian Rost,<sup>1</sup> Andy Nowacki<sup>1</sup> and Sanyi Yuan<sup>3</sup>

**4** <sup>1</sup> *School of Earth and Environment, University of Leeds, Leeds, LS2 9JT, UK*

**5** <sup>2</sup> *ESG Solutions, Kingston, ON K7K 7K2, Canada*

**6** <sup>3</sup> *College of Geophysics and Information Engineering, China University of Petroleum, Beijing, 102249, China*

**7** <sup>4</sup> Received 2017 \*\*\*\* \*\*; in original form 2017 October 18

### **5 SUMMARY**

**6** With the proliferation of dense seismic networks sampling the full seismic wavefield, recorded  
**7** seismic data volumes are getting bigger and automated analysis tools to locate seismic events  
**8** are essential. Here, we propose a novel Multichannel Coherency Migration (MCM) method  
**9** to locate earthquakes in continuous seismic data and reveal the location and origin time of  
**10** seismic events directly from recorded waveforms. By continuously calculating the coherency  
**11** between waveforms from different receiver pairs, MCM greatly expands the available infor-  
**12** mation which can be used for event location. MCM does not require phase picking or phase  
**13** identification, which allows fully automated waveform analysis. By migrating the coherency  
**14** between waveforms, MCM leads to improved source energy focusing. We have tested and  
**15** compared MCM to other migration-based methods in noise-free and noisy synthetic data. The  
**16** tests and analysis show that MCM is noise resistant and can achieve more accurate results  
**17** compared with other migration-based methods. MCM is able to suppress strong interference  
**18** from other seismic sources occurring at a similar time and location. It can be used with ar-  
**19**bitrary 3D velocity models and is able to obtain reasonable location results with smooth but  
**20**inaccurate velocity models. MCM exhibits excellent location performance and can be easily

2 *Peidong Shi et al.*

21 parallelized giving it large potential to be developed as a real-time location method for very  
22 large datasets.

23 **Key words:** Earthquake source observations – computational seismology – time-series anal-  
24 ysis – earthquake monitoring and test-ban treaty verification.

25 **1 INTRODUCTION**

26 With the routine deployment of large monitoring arrays, significant quantities of waveform data  
27 have and are being recorded by various types of seismometers and geophones around the world.  
28 The increasing volume of real-time seismic data and the necessity to seismically monitor natu-  
29 ral and man-made seismic hazard require the development of fully automated seismic analysis  
30 methods. Conventional arrival time based source location methods require accurate picking of the  
31 P- and/or S-wave arrivals. However, even though automatic picking algorithms are being used  
32 increasingly (Allen 1982; Bai & Kennett 2000; Saragiotis et al. 2002; Yuan et al. 2018), man-  
33 ual picking is still usually needed to increase location accuracy as well as quality control. This  
34 kind of user interactivity is expensive, time consuming and cannot handle the increasingly larger  
35 datasets resulting from full wavefield experiments. Furthermore, picking algorithms do not work  
36 well when the signal-to-noise ratio is too low and/or the phase arrivals of different seismic events  
37 overlap. Therefore arrival time based location methods are more suitable for locating global and  
38 regional earthquakes with recognisable phase arrivals. Conversely, microseismicity such as small  
39 tremors during volcanic activity, induced seismicity during fluid injection and triggered/induced  
40 seismicity during reservoir depletion have relatively smaller magnitudes. The recorded amplitudes  
41 of these microseismic events are weak and often inundated by noise. Additionally for hydraulic  
42 fracturing, a large number of microseismic events can occur in a limited spatial and temporal  
43 window, which often causes interference of the recorded waveforms. As such, the detection and  
44 location of microseismic events can be extremely difficult, making conventional arrival time based  
45 location methods not ideal for locating microseismic events.

\* Corresponding author: Peidong Shi. Email: eepsh@leeds.ac.uk. Fax: +44 113 343 5259

The conventional picking and arrival time based methods only utilize the traveltime information while valuable information in the data such as recorded waveforms are omitted. Furthermore, effectively utilizing the available waveforms and extracting useful information from the recorded data are important to comprehensively evaluate the seismic source. In order to make full use of the recorded wavefield, waveform-based methods are increasingly used to automatically locate the microseismicity and characterize the source mechanism. Cesca & Grigoli (2015) reviewed the recent application of full waveform methods in microseismic location, source mechanism characterization and microseismicity waveform classification. Phase picking and identification are not required in the waveform-based location methods, which enable their application on data with low signal-to-noise ratio. Waveform-based location methods can be divided into two main categories: migration-based location methods and full waveform inversion methods. Full waveform inversion approaches are often used to determine the velocity model of the subsurface (Tarantola 1984) and can also be used to characterize source parameters (Wu & McMechan 1996; Ramos-Martínez & McMechan 2001; Kaderli et al. 2015). However due to the high computational cost, it is not extensively used in seismic source characterization. The migration-based methods can be divided into reverse time imaging and diffraction stack imaging (DSI) approaches (McMechan 1982; Fink et al. 2000; Larmat et al. 2006; Kao & Shan 2004; Liao et al. 2012; Drew et al. 2013; Grigoli et al. 2013a). Reverse time imaging approach utilizes the reversibility of the wave equation and propagates the recorded seismograms backward in time to resolve the source parameters (Steiner et al. 2008; Larmat et al. 2009; Artman et al. 2010); it involves solving the wave equation and thus is computationally intensive. Constructing an appropriate imaging condition and imaging seismic sources having different radiation patterns are also challenges for reverse time imaging. DSI approaches use delayed and summed coherent phases from different station recordings according to traveltimes of P- and/or S-phases for a specific velocity model to focus the source energy at the estimated source location. It is computationally faster and can be applied to arbitrarily complex media. However the DSI approach cannot effectively utilize the whole wavefield, and reflections, multiples and mode conversions often make this method unsuitable.

For the DSI method, Kao & Shan (2004) first proposed a source scanning algorithm (SSA) in

74 which the absolute amplitudes of normalized seismograms in a selected time window are stacked  
75 to image the seismic sources with emergent arrivals in both space and time. At the correct source  
76 position and origin time, the waveform will add coherently, which will lead to maximum energy  
77 focusing. Through identifying the maximum value in the stacked data volume, both the location  
78 and origin time of the source can be determined. For a pure shear source, the source radiation  
79 pattern will cause difficulty in imaging the source directly from original waveform data. The max-  
80 imum value of the stacked data will not appear at the true source location due to the radiation  
81 pattern of seismic source and thus influencing the accuracy of the location (Artman et al. 2010;  
82 Zhebel & Eisner 2014). Thus varieties of modified DSI methods have been proposed to eliminate  
83 the influence of the source radiation pattern. Kao & Shan (2007) further modified the SSA by  
84 stacking the P-wave envelopes to rapidly image the rupture pattern of an earthquake. Grigoli et al.  
85 (2013b) stacked the short-term-average/long-term-average (STA/LTA) traces to locate mining in-  
86 duced seismicity and also estimated the location uncertainties. As an estimated velocity model is  
87 required to migrate recorded waveforms in the DSI, the location performance of the DSI approach  
88 often strongly depends on our knowledge of the subsurface velocity model. To overcome the dif-  
89 ficulty of obtaining an accurate velocity model, Grigoli et al. (2016) proposed the master-event  
90 waveform stacking to reduce the dependency of DSI on velocity model. However for DSI, to fur-  
91 ther utilize the waveform information and obtain high-quality imaging results on extremely low  
92 signal-to-noise data the method still requires improvements.

93 In seismology, cross-correlation is often used to evaluate the coherency between waveforms  
94 from different stations (Wang et al. 2016). It has been widely used to estimate signal delay times  
95 (VanDecar & Crosson 1990) and in seismic interferometry (Halliday & Curtis 2008; Wapenaar  
96 et al. 2011). Wassermann & Ohrnberger (2001) utilized the wavefield coherency to determine  
97 the hypocenter of volcano induced seismic transients. Recently Ruigrok et al. (2016) performed  
98 beamforming based on cross-correlated data. Here, we propose a Multichannel Coherency Migra-  
99 tion (MCM) method to determine the location and origin time of seismicity. In the MCM method  
100 the coherency between different receiver pairs are stacked to focus the source energy. The co-  
101 herency between all possible receiver pairs are calculated simultaneously through normalizing

the covariance matrix of the recorded waveforms. We will first introduce the theory of the new proposed location method. Then we compare the MCM method with different migration-based location methods in the presence of strong random noise for a synthetic full waveform dataset. The location results demonstrate that the MCM can achieve a better imaging resolution under varying noise levels. Finally, we show that the MCM can obtain more stable and reasonable location results compared with other migration-based location methods when the velocity model is not accurate or strong interference exists. The applications of MCM on real datasets and practical situations can be found in Shi et al. (2018b).

## 2 METHOD

In this section, we will first describe previously used migration techniques and then introduce our new location method. Migration-based location methods often consist of four components: (1) traveltime calculation, (2) characteristic function calculation, (3) migration and (4) source event identification.

### 2.1 Constructing the traveltime table

The rupture lengths of microseismic events are significantly smaller compared to the dominant wavelength of seismic waves, especially for surface monitoring. Thus microseismic sources can be well approximated as point sources. In the potential source location region, the volume can be discretized into image points according to the required spatial resolution. The spatial interval should be less than one half-wavelength to ensure a sufficient spatial sampling rate. Once the source and receiver geometry is determined, a look-up table of traveltimes is constructed for both P- and S-waves given the seismic velocity model. The look-up table only needs to be calculated once in the whole location process, thus accelerating the migration of waveforms later.

The traveltime calculation of direct P- and S-wave can be expressed as  $t^P(x, y, z) = f(v_P, G)$  and  $t^S(x, y, z) = f(v_S, G)$  respectively, where  $v_P, v_S$  represent the P- and S-wave velocity fields,  $G$  represents the geometry of potential source locations and receiver array and  $x, y, z$  are 3D spatial coordinates of the source point. The traveltime table can be built upon any known velocity

model of arbitrary complexity and seismic traveltimes can be calculated using the seismic wave equation in a variety of ways. In homogeneous medium, the traveltimes can be calculated using analytical solutions; in 1D layered media, the traveltimes can be calculated e.g. using ray-tracing or the reflectivity method; in 2D and 3D heterogeneous media, the traveltimes can be calculated e.g. using an Eikonal solver (Podvin & Lecomte 1991).

## 133 2.2 Calculating the characteristic function

Unlike exploration seismology, where explosive sources are extensively used, tectonic events show complex rupture patterns and therefore show different radiation patterns for the seismic energy. Due to the radiation pattern, the polarization of the P- and S-waves vary dependent on the take-off and azimuth angles of the seismic energy, which means the polarization of these recorded phases may vary in amplitude and sign for different receivers along the array. Thus simply stacking the amplitude of recorded waveforms may contribute to an inaccurate imaging result, leading to several maxima around the true source position. This is especially significant when imaging pure double-couple sources using only single phase and single component data (Artman et al. 2010; Zhebel & Eisner 2014). The polarization needs to be taken into account when migrating energy back to the source location to avoid ambiguous imaging results. In order to remove the influence of the source radiation pattern, various characteristic functions have been used to perform waveform migration, e.g. the absolute value (Kao & Shan 2004), the envelope (Kao & Shan 2007; Gharti et al. 2010), the STA/LTA (Drew et al. 2013; Grigoli et al. 2013b) and the kurtosis of the waveforms (Langet et al. 2014).

The characteristic function is actually a transformation of the recorded original waveforms in order to obtain non-negative stacking traces. The transformation can be expressed as  $S(t) = \mathcal{T}(d(t))$ , where  $d(t)$  represents the recorded original data,  $\mathcal{T}$  corresponds to different kinds of transformations,  $S(t)$  represents the characteristic function after transformation. Stacking the envelope or the absolute value of the waveforms cannot effectively utilize the non-correlation of the random noise and so often fails to suppress random noise. Thus these kinds of characteristic functions only work well on data with high signal-to-noise ratio. The STA/LTA or kurtosis of the

waveforms utilizes the statistical characteristics of the data and is often used to detect and pick weak signals (Allen 1982; Saragiotis et al. 2002). Thus the STA/LTA and kurtosis characteristic functions have the ability to suppress random noise in the data. However the performance of the STA/LTA or kurtosis transforms are often subject to the choice of time window and are often unsatisfactory in low signal-to-noise ratio situations. The STA/LTA and kurtosis transforms can highlight weak signals against background noise, but at the expense of losing accurate estimation of the source magnitude.

## 2.3 Migration

### 2.3.1 Conventional migration

After the traveltime table and characteristic function have been calculated, traditional waveform migration can then be performed upon each potential source location and estimated origin time. At each potential source location, migration is performed by summing the windowed characteristic functions according to the travelttime table and estimated origin time. By stacking the characteristic function, the source energy will focus at the true source location and correct source origin time. Thus a 4D imaging function  $W(x, y, z, t_0)$  is obtained, where the maximum corresponds to the estimated source location and origin time:

$$W(x, y, z, t_0) = \sum_i^N \sum_R^R |S_i(\tau_R^P)| + \sum_i^N \sum_R^R |S_i(\tau_R^S)|, \quad (1)$$

where  $i$  represents the  $i$ th component of the recorded data,  $W(x, y, z, t_0)$  is the 4D imaging function that corresponds to the spatial location and origin time of the source,  $\tau_R^P$  and  $\tau_R^S$  represent the delayed P- and S-wave traveltimes from a specified image point  $(x, y, z)$  to the receiver  $R$ .  $\tau^P$  and  $\tau^S$  can be explicitly expressed as

$$\tau^P(x, y, z, t_0) = t^P(x, y, z) + t_0 \quad \text{and} \quad \tau^S(x, y, z, t_0) = t^S(x, y, z) + t_0, \quad (2)$$

where  $t_0$  is the delay time which accounts for the origin time of the source. The P and S phases are simultaneously used in the migration method to better constrain the source location (Gharti et al. 2010). It is feasible to include multiple phases into the migration, which might significantly improve the resolution of the source location. However the accuracy of the traveltimes for reflected

and converted phases depends more heavily on the velocity model than the primary phases. If an accurate velocity model is available, reflections and conversions could be incorporated into the migration method to improve the imaging quality. Usually the P-waves will have a distinct arrival on the vertical component record while the S-waves tend to have a distinct arrival on the horizontal component record. Thus, jointly utilizing multi-component data in migration is also recommended, as it can provide more information and constraints for source location.

### 2.3.2 Multichannel Coherency Migration

Unlike conventional migration methods which directly migrate the waveforms of the original data or the characteristic functions of recorded waveforms, our MCM first calculates the Pearson correlation coefficients (Ezekiel & Fox 1959) of time windowed records for all possible combinations of two or more stations and then stacks the calculated correlation coefficients. The time window used for coherency analysis is determined according to the length of the source time function and thus will include both the direct P- and S-phases at the correct source position and origin time. The approach works with imaging either P or S arrivals or a combination of both. The Pearson correlation coefficient describes the linear dependence between two or more traces, and can be calculated based on two-channel or multichannel (which can be interpreted as multidimensional cross-correlation Arfken & Weber (1999)) as

$$r_m = \frac{\sum_t [w_{i_1}(d_{i_1}(t) - \overline{d_{i_1}(t)})] [w_{i_2}(d_{i_2}(t) - \overline{d_{i_2}(t)})] \cdots [w_{i_n}(d_{i_n}(t) - \overline{d_{i_n}(t)})]}{\sigma_{i_1} \sigma_{i_2} \cdots \sigma_{i_n}}, \quad (3)$$

where  $r_m$  is the  $m$ -th multidimensional waveform coherency ( $n$ -dimension) among different stations  $i_1, i_2, \dots, i_n$  ( $i_j \in [1, 2, \dots, N]$ ) and  $N$  is the total number of all stations,  $m \in [1, 2, \dots, M]$  and  $M$  is the total number of n-wise groups of stations),  $d_{i_j}(t)$  is the time windowed signal of the  $i_j$ -th station according to the pre-calculated travelttime table and estimated origin time,  $w_{i_j}$  is weighting factor for the  $i_j$ -th station,  $\sigma$  is the standard deviation of the corresponding signal and the overlines denote averages. When the data quality of a trace is good, the weighting factor  $w_{i_j}$  is set to 1; whereas when a trace is highly contaminated by noise, the weighting factor  $w_{i_j}$  is set to 0. The weighting factors can be adjusted but in our test we retain with these binary weightings. By

207 exploiting weighting factors, known-good or known-bad traces can be up-/down-weighted. The  
 208 correlation coefficient of two input signals is equal to the covariance of the two signals normalized  
 209 by the product of their standard deviations. The correlation coefficient evaluates the waveform  
 210 similarity among the traces and has a value between +1 and -1, where  $\pm 1$  represents a total pos-  
 211 itive/negative linear correlation between the two traces, whilst 0 represents no linear correlation  
 212 between two traces. If the waveforms of the two traces within the selected time window are sim-  
 213 ilar, such as for coherent P arrivals, the absolute value of the correlation coefficient will be high  
 214 towards 1. If the waveforms of the two traces within the selected time window are not coherent,  
 215 such as for random noise, the absolute value of the correlation coefficient will be low towards  
 216 0. Fig. 1 shows the corresponding waveform coherency within a time window at the true source  
 217 location and an incorrect position respectively. At a particular imaging point, by the utilization  
 218 of multidimensional waveform coherency, the total number of effective information available for  
 219 migration is improved from  $N$  to  $M = \frac{N!}{L!(N-L)!}$  ( $L = \sum_{i,j} w_{ij}$  and ! denotes factorial).

220 When calculating the coherency between waveforms, the cross-correlation method is exten-  
 221 sively used (such as the cross-correlation beamforming method proposed by Ruigrok et al., 2016).  
 222 The zero-lag normalized cross-correlation can be expressed as

$$r_{ij} = \frac{\sum_t (d_i(t)d_j(t))}{|d_i(t)||d_j(t)|}, \quad (4)$$

223 where  $|\cdot|$  represents the norm of the waveform vector. The normalized cross-correlation can  
 224 achieve similar results to the standard correlation coefficient when the input waveforms all have  
 225 zero mean values. However, when the recorded waveforms of some stations are biased (e.g. due to  
 226 different instrument responses or different waveform processing), the normalized cross-correlation  
 227 will not effectively evaluate the coherency between waveforms, while the correlation coefficient  
 228 may still calculate the coherency accurately as the mean values have been removed from the input  
 229 waveform data and the covariance is normalized by the standard deviation of the input data.

230 Next the absolute value of the correlation coefficients of the traces are stacked to image the  
 231 source location and origin time. The influence of the source radiation pattern can be eliminated  
 232 by stacking the absolute value of the correlation coefficients. The stacked traces (referred to as

<sup>234</sup> stacking function hereafter) can be expressed as

$$\text{<sup>235</sup>} \quad p(x, y, z, t_0) = \frac{1}{2M} \left( \sum_{m=1}^M |r_m^P| + \sum_{m=1}^M |r_m^S| \right), \quad (5)$$

<sup>236</sup> where  $r_m^P$  and  $r_m^S$  represent the waveform coherency of P- and S-phases respectively,  $M$  is the  
<sup>237</sup> total number of unique multichannel receiver groups,  $p(x, y, z, t_0)$  is the final 4D imaging function  
<sup>238</sup> and stores the stacked waveform coherency at position  $(x, y, z)$  and origin time  $t_0$ . The imaging  
<sup>239</sup> function  $p(x, y, z, t_0)$  is a bounded function, with values between 0 and 1. The stacked correlation  
<sup>240</sup> coefficients are normalized by the total number of unique multichannel receiver groups given by  
<sup>241</sup>  $M$ . Here, because both P- and S-phase coherency are used, the stacked correlation coefficients  
<sup>242</sup> are thus normalized by  $2M$ . If the waveforms of all the traces in the selected time window are  
<sup>243</sup> completely linearly coherent (positive or negative correlation), then the correlation coefficients are  
<sup>244</sup> all 1 and the final imaging value for this point and origin time is  $p = 1$ . With seismic data, because  
<sup>245</sup> of noise and heterogeneity of the medium, the stacked coherency of the source may rather have a  
<sup>246</sup> high value approaching 1.

### <sup>247</sup> 2.3.3 Two-dimensional MCM

<sup>248</sup> In equation 3, if  $n$  is chosen to be 2, we can obtain the most concise form of MCM, i.e. two-  
<sup>249</sup> dimensional MCM. The Pearson correlation coefficient between two traces is calculated by

$$\text{<sup>250</sup>} \quad r_{ij} = \frac{\sum_t w_i w_j [d_i(t) - \bar{d}_i(t)] [d_j(t) - \bar{d}_j(t)]}{\sigma_i \sigma_j}, \quad (6)$$

<sup>251</sup> where  $r_{ij}$  is the correlation coefficient (i.e. coherency) between waveforms from station  $i$  and  $j$ ,  
<sup>252</sup>  $d_i(t)$  and  $d_j(t)$  are the two input waveforms within the selected time window. Correspondingly,  
<sup>253</sup> the stacking function can be expressed as

$$\text{<sup>254</sup>} \quad p(x, y, z, t_0) = \frac{1}{N(N-1)} \left( \sum_{i < j}^N |r_{ij}^P| + \sum_{i < j}^N |r_{ij}^S| \right). \quad (7)$$

<sup>255</sup> In equation 7, because both P- and S-phase coherency are used, the stacked correlation coefficients  
<sup>256</sup> are normalized by twice the total number of unique receiver pairs which is  $N(N-1)/2$ .

<sup>257</sup> The calculation of the two-dimensional MCM can be expressed in matrix form yielding an  
<sup>258</sup> efficient computational algorithm. The coherency does not need to be calculated based on each

259 receiver pair separately. In other words, the correlation coefficients between all possible receiver  
 260 pairs can be calculated simultaneously through forming a covariance matrix. At each imaging  
 261 point a data matrix  $\mathbf{D}$  can be constructed from the recorded data according to the pre-calculated  
 262 traveltime table and estimated origin time. The data matrix  $\mathbf{D}$  has the dimensions  $[N_t \times N]$  ( $N_t$  is  
 263 the length of the time window):

$$264 \quad \mathbf{D} = [\mathbf{d}_1 \mathbf{d}_2 \cdots \mathbf{d}_N], \quad (8)$$

265 where  $\mathbf{d}_i$  is a column vector and represents the windowed signal of the  $i$ th trace. The covariance  
 266 matrix  $\mathbf{C}$  is then calculated through

$$267 \quad \mathbf{C} = \widehat{\mathbf{D}}^T \widehat{\mathbf{D}}, \quad (9)$$

268 where  $\widehat{\mathbf{D}} = \mathbf{D} - \mathbf{E}\mathbf{D}/(N - 1)$  represents the signal deviations from their individual expected  
 269 values ( $\mathbf{E}$  is a  $N_t \times N_t$  square matrix with all elements equal to 1) and  $T$  represents transpose. The  
 270 correlation coefficient matrix can be obtained through

$$271 \quad \mathbf{R} = \frac{\mathbf{C}}{\boldsymbol{\sigma}\boldsymbol{\sigma}^T}, \quad (10)$$

272 where  $\boldsymbol{\sigma}$  is the standard deviation vector (i.e.  $\boldsymbol{\sigma} = [\sigma_1 \sigma_2 \cdots \sigma_N]^T$ ). Here the division in equation 10  
 273 means element-wise division not matrix division. Finally the stacking coherency at this imaging  
 274 point and origin time is

$$275 \quad p = \frac{\sum_{i < j}^N (|\mathbf{R}_P| + |\mathbf{R}_S|)}{N(N - 1)}, \quad (11)$$

276 where  $\mathbf{R}_P$  and  $\mathbf{R}_S$  represent the correlation coefficient matrix of the P- and S-waves respectively.  
 277 The summation in equation 11 is performed over the upper-triangular elements of the correlation  
 278 coefficient matrix to exclude the auto-correlation of the signals.

279 The application of the MCM can be quite flexible. The waveform coherency can be easily cal-  
 280 culated based on two or more traces. Using the coherency of multiple traces, the source coherency  
 281 can be further strengthened. The selected time window can also be altered adaptively during the  
 282 coherence analysis. The MCM can be applied to the original waveform data as well as any kind of  
 283 the characteristic functions of the original data. As the original waveform data normally contain  
 284 the most abundant information, applying MCM directly to the waveform data is recommended. In

285 this paper, our MCM results and analysis are all based on the coherency of the original waveform  
 286 data for two stations.

287 **2.4 Identifying the source location and origin time**

288 Once the migration process is done, a 4D migration volume is finally generated, which contains  
 289 the information about source location and origin time. If there is only one seismic event recorded  
 290 in a certain monitoring time period, the location  $(x_s, y_s, z_s)$  and origin time  $t_{0s}$  of this event can  
 291 be identified through finding the maximum value in the 4D image volume  $p(x_s, y_s, z_s, t_{0s}) =$   
 292  $\max\{p(x, y, z, t_0)\}$ . If multiple events exist, events can be identified by setting a coherency thresh-  
 293 old. The coherence threshold is determined through investigating the stacking coherency of the  
 294 background noise. Any stacking coherency above the threshold can be viewed as a seismic event.  
 295 However, when the imaging point and estimated origin time are close to the true source location  
 296 and origin time, high coherency will also appear in the imaging domain. In order to avoid mis-  
 297 identification of non-physical sources, only one seismic event with the highest coherency will be  
 298 identified within a specific space zone and time period. Fig. 2 shows the workflow for the conven-  
 299 tional migration-based location method and the MCM location method.

300 In theory, the origin time of the source corresponds to the time of maximum stacking energy.  
 301 The stacking energy rises above the coherency level of background noise as the coherency analysis  
 302 time window approaches the origin time of the source (a coherency analysis time window earlier  
 303 than the origin time), reaches a maximum value around the origin time and then decreases to the  
 304 coherency noise level as the window passes the end time of the source wavelet. Fig. 3 shows two  
 305 signals with random noise and the calculated coherency between the two noisy signals using a  
 306 sliding time window. In this example, the two signals are negatively correlated. A constant shift in  
 307 amplitude is added to one signal. Random noise is added to the two signals separately. Fig. 3(b)  
 308 displays the coherency of the two signals calculated through the Pearson correlation coefficient  
 309 method expressed in equation 3. Fig. 3(c) displays the coherency of the two signals calculated  
 310 through the normalized cross-correlation method expressed in equation 4. We can see the co-

311 herency is better evaluated by the Pearson correlation coefficient method when the waveforms  
 312 have differing means.

313 We can see that the coherency functions of the synthetic data have a flat maximum (Fig. 3(b)).  
 314 The flat maximum lasts one period of the source time function plus the length of the coherency  
 315 analysis time window. Thus the determination of the origin time from the stacking function needs  
 316 to be calibrated based on the coherency analysis time window. If the length of the time window  
 317 is chosen to be the same as the period of the signal, the flat maximum is symmetrical about the  
 318 origin time (second row in Fig. 3(b)). The length of the time window influences the performance  
 319 of the coherency function in the presence of noise. A longer time window suppresses noise well  
 320 since more samples are used in calculating the coherency between different traces (see Fig. 3(b)).  
 321 However a longer time window will reduce the spatial and temporal resolution of the imaging  
 322 result, as interference easily happens when more data are incorporated into coherency analysis.  
 323 And the coherency value of the windowed data will also decrease due to the longer time window,  
 324 as more non-coherent samples are taken into the coherency analysis. Thus when choosing the time  
 325 window, the trade-off between noise suppression and imaging resolution needs to be considered.  
 326 In practice, a time window which equals the length of the source wavelet is suggested as it can  
 327 keep a balance between the noise suppression and imaging resolution. However, when the noise  
 328 is very strong in the recorded data, a longer time window is expected to be more appropriate. In  
 329 the following sections, we will use approximately one period of the recorded signals as the time  
 330 window since it will provide the optimal temporal resolution of the origin time.

### 331 3 NOISE RESISTANCE

332 For microseismic monitoring, locating weak seismic events is challenging. The signals from weak  
 333 or small events are more likely to have lower signal-to-noise ratios. In contrast to traditional single-  
 334 channel based migration methods, the two-dimensional MCM method utilizes the resemblance  
 335 between different receiver pairs and increases the number of available data from  $N$  to  $N(N - 1)/2$   
 336 ( $N$  is the total number of traces). Thus the MCM method is more resistant to noise and hence  
 337 able to identify weak events, which is critical for enhancing microseismic monitoring. In order to

evaluate the performance of different migration-based location methods in the presence of noise, we compare the stacking functions of different migration methods at the source position using different noise-to-signal ratios (as shown in Fig. 4). The noise-to-signal ratio (NSR) is defined by the ratio of the maximum amplitude between noise and signal, which is used to highlight the noise level more intuitively. Here four migration-based location methods are compared, i.e. using the waveform envelope, STA/LTA and kurtosis as characteristic functions and our MCM method as defined in section 2.3.2.

Source prominence ( $S_{pro}$ ) is used to evaluate the performance of the different methods in source identification. The source prominence is defined as the ratio of the stacked energy of the source to the average stacked energy of the noise, and is a unitless metric that characterises how strong the source coherency is with respect to the background noise. The higher the source prominence is, the greater the certainty in the source location and origin time estimates. As the NSR increases, the stacked energy of the background noise also increases, and so source identification is more difficult. When the NSR reaches approximately 12, only the MCM method can accurately locate the source, while all the other methods fail (Fig. 4(c)). As shown in Fig. 4(d), the source prominences of the MCM are larger and also decrease more slowly with increasing NSRs compared to the other methods, which confirms the improved noise resistance of the MCM method. As statistic-based migration methods, the STA/LTA and kurtosis methods show better performance than the envelope method and their source prominences are higher than the envelope method. However, when NSR is higher than 3, the source prominence of kurtosis method decreases rapidly. And when NSR is higher than 4, the performance of the kurtosis method is not as good as the STA/LTA method and even inferior to the envelope method. Compared to the other methods, the kurtosis method is more sensitive to strong noise.

Source prominence is sensitive to the NSR. High NSR will lead to a high background noise level, thus contributing to a low source prominence. As indicated in Fig. 4, source prominence could be used to evaluate the noise resistance ability of a source location method. Fig. 5 exhibits the source prominence of the MCM method under different NSRs. We can see that the source prominence decreases gradually with increasing NSR. The source prominence eventually

approaches 1 with extremely high NSR, which means the source energy is completely inundated by the background noise. We use a Monte Carlo simulation to obtain the variation of the source prominence with different NSRs. For every different NSR, the source prominence is obtained by calculating the average prominence of 10 separate data with independent random noise. From Fig. 5(d), we can infer a relation between the source prominence and the NSR, which can be expressed as  $S_{pro} = \alpha * \exp(\beta * NSR) + 1$ . The scale factor  $\alpha$  and  $\beta$  will depend on the radiation pattern of the source, time window length of the coherency calculation and the frequency content of the signal and noise. Since increasing the total number of traces only contributes to increasing the number of available coherency information having the same coherency level, in theory the source prominence is not affected by the total trace number ( $N$ ).

Another important property to evaluate the noise resistance ability of a migration-based location method is the variation of the stacked energy of the background noise ( $\sigma_{noise}^2$ ). When the source prominence is low, the variation of the noise energy will be extremely important for determining the correct source location. The stacked noise energy could form several local maxima in the stacking function, which will hinder precise source identification. The lower the variance of the stacked noise energy, the easier it will be to identify the source. Fig. 6 shows the stacking functions and variance of noise energy at the source position for different number of traces ( $N$ ) and the different methods. The available trace number ranges from 10 to 100. We can see the variance of the noise decrease gradually with increasing number of traces for all four methods. The MCM method has the lowest variance of noise energy for all trace numbers  $N$ , indicating better performance of the MCM method on source location and origin time estimation. The noise variance of STA/LTA and kurtosis methods fall between the MCM and envelope methods.

The variance of the stacked noise energy is sensitive to the total number of available traces  $N$ . For  $N$  receivers, there are  $N(N - 1)/2$  unique receiver pairs, which can provide effective coherency information. Increasing the number of receivers could effectively reduce the variance of noise energy in the stacking function. Fig. 7 shows that the variance of noise energy decreases rapidly with an increasing number of traces. A low variance of noise energy makes it much easier to identify the source location and origin time. From Fig. 7(d), we can estimate the relationship

394 between the variance of noise energy and the number of traces, which is  $\sigma_{noise}^2 = a/(N(N - 1))$ .  
 395 This means the variance of noise energy is inversely proportional to the number of unique receiver  
 396 pairs. The scale factor  $a$  is related to the statistical characteristics and frequency content of the  
 397 noise.

398 In order to test the performance of different methods in the presence of strong noise, we use a  
 399 synthetic full waveform microseismic dataset. Fig. 8 shows the velocity model and the geometry  
 400 of the surface array. A pure dip-slip source is located in the middle of the layered earth model, with  
 401 coordinates of 2.0, 2.0 and 2.85 km in the X, Y and Z directions, respectively. The receivers are  
 402 uniformly distributed on the free surface with a constant spacing of 0.2 km and are symmetrical  
 403 about the epicenter of the source. The synthetic data for this model and source-receiver geometry  
 404 are shown in Fig. 9. Gaussian random noise has been added to the synthetic data. A NSR of 6  
 405 is used and represents a relatively high noise level. From Figs 9(a) and 9(c), we can see that the  
 406 effective signals have been completely masked by the random noise, and hence we cannot identify  
 407 the direct P- and S-waves within the waveform data. Manual picking of the direct P- and S-wave  
 408 arrivals is impossible with such a high noise level.

409 The coordinates of the target area are set between 1 to 3 km in the X and Y directions, and  
 410 between 2.2 to 3.5 km in the Z direction. This target volume is discretized with 45387 potential  
 411 source positions with 50 m grid interval in the X, Y and Z directions. A total of 1001 origin  
 412 times are scanned with a time interval of 1 ms. Fig. 10 shows the vertical and horizontal slices  
 413 through the stacking functions at the maximum for the four migration-based location methods.  
 414 The color in the figures exhibits the maximum-likelihood location of the source. As shown in Fig.  
 415 10, only the MCM can identify the true source location in the presence of the high noise level.  
 416 The STA/LTA method locates the source correctly in the X and Z directions, but deviates 50 m  
 417 in the Y direction. Both the envelope and kurtosis methods have very large deviations and fail to  
 418 locate the correct source location in this situation. 3D profiles of the STA/LTA and MCM migration  
 419 results are further displayed in Fig. 11. Compared with the STA/LTA migration results, migration  
 420 results of the MCM method have a more distinguishable source imaging effect with better source  
 421 prominence and no location errors.

Fig. 12 shows the stacking functions at the correct source location for all the methods. Only the MCM and the STA/LTA methods have a recognisable stacked energy around the origin time of the source. The MCM method has a better source prominence compared with the other methods. Table 1 shows the location error of the different methods, and demonstrates the robustness of the MCM method over the other methods in terms of noise resistance.

#### 4 ROBUSTNESS AND IMAGING WEAK EVENTS

Given the complexity of the fracturing process as well as geological heterogeneity, it is quite common that weak seismic events occur spatially with strong events within roughly the same time period (e.g. Gutenberg–Richter law). Imaging extremely weak events in the presence of larger events is difficult, because the signals of the large events have much larger amplitude and signal-to-noise ratio than the weak events. Furthermore, the reflected waves, multiples and coda waves of the large events potentially interfere with weak events, especially in complex geological structures. The robustness against interfering signals is critical for imaging weak events. In this section we test and compare the ability to image extremely weak events using different migration methods.

For pure amplitude-based migration methods, such as migration using amplitude, envelope and energy of the traces, the imaging results are often dominated by strong amplitude signals. From equation (3), we can see that the covariance between traces is normalized by the standard deviation of the traces. Thus the coherency between traces is not affected by the absolute amplitude of the recorded phases, and rather only affected by the resemblance of the waveforms. In this way, the MCM can resist interference from large events and balance the imaging results between strong and weak events. In fact the imaging quality of the events in the MCM method is not affected by the absolute amplitude of the events, but mainly influenced by the signal-to-noise ratio of the signals of the corresponding events. Even though the signal of large events have higher signal-to-noise ratios, they are not largely coherent at the true locations of other weak events. Thus the overall coherency of the large event interference is not comparable with respect to the local coherency of the weak signals. For the statistic-based migration methods based on characteristic functions of a single trace, such as the STA/LTA and kurtosis methods, strong interference signals over large

scales can lead to non-physical source images. However, for the MCM method, as long as the interference signals are not coherent over a large scale between traces, the interference will not locally focus in the imaging domain.

The robustness of the different migration methods in resisting strong interference is tested using synthetic waveform traces. Fig. 13 shows the time aligned traces and the stacking functions at the correct source location. We have added large coherent interference signals into 23 of the traces (Fig. 13(b)). The amplitude of the interference signals is 32768 times the amplitude of the weak signals to be detected, chosen to make the seismic magnitude of the events 3 times larger. With such an extremely strong energy contrast, only the MCM method correctly locates the weak signals and suppress the large interference signals at the same time (Fig. 13(c)). The results of the other methods are dominated by the large interference signals. The STA/LTA method can successfully detect the weak signals, however shows an even stronger indication of the large interference signals. Here we have added coherent interference signals, but if the interference signals in different traces are not coherent, even more significant interference suppression can be expected for the MCM method.

Fig. 14 shows the same velocity and geometry model as used in Fig. 8 but with two double-couple sources placed at depths of 2.55 and 3.15 km, respectively. Event 1 is a vertical dip-slip source with an origin time of 0 s and event 2 is a 45 degree dip-slip source with an origin time of 0.1 s. Event 1 and event 2 have the same source time function, which means the recorded signals of event 1 and 2 are coherent. In this situation, imaging the source events will be more difficult for the MCM. The seismic moment of event 1 is 1024 times that of event 2, such that the magnitude of event 1 is twice as large. In Fig. 14(b), the amplitudes of the P- and S-waves from event 1 are so large that we can hardly identify the P- and S-wave arrivals of event 2. The multiples and reflected waves from event 1 have much larger amplitude than the direct waves of event 2.

Fig. 15 shows the vertical and horizontal slices through the true location of event 1 for the four migration-based location methods. Because event 1 has a much larger magnitude, we obtain very good energy focusing of event 1 for all four methods. The vertical profiles of the envelope, STA/LTA and kurtosis methods show a similar pattern around the location of event 1, which is

related to the source-receiver geometry. The resolution of STA/LTA is lower compared with the other methods. It is worth noting that for the STA/LTA method, the maximum stacking value is not at the correct location of event 1, and is 1 grid point deeper. This leads to a 50 m location deviation for event 1, while the other methods all locate accurately. The poor performance of the STA/LTA method is likely due to the relatively lower resolution in the vertical direction, which results from the inaccurate estimation of the origin time of the event.

Fig. 16 shows vertical and horizontal slices through the true location of event 2 for the four migration-based location methods. Due to strong interference from event 1 and the weak amplitudes of event 2, the energy focusing of event 2 is not as good as event 1. The interfering energy from event 1 can be seen in the migrated profiles, and significantly influences the correct location of event 2. Compared to other methods, the MCM method is better at suppressing the strong interference from event 1 and so results in good imaging results for the vertical profiles. In the horizontal section (the bottom right one in Fig. 16), it is apparent that the MCM methods suffers strong interference from event 1. However the energy focusing for event 2 is still recognisable. In this situation, a well-designed source identification algorithm is needed to correctly identify the weak event. We can see it is very hard to simultaneously image seismic events whose signals are interfering and which have magnitude differences larger than 2. Here the signals of event 1 and 2 are coherent. If they are not coherent, a better imaging result of event 2 can be achieved using the MCM method.

Fig. 17 shows the stacking functions at the true locations of event 1 and 2. The four methods all exhibit very good migration results for the strong event 1. However for the weak event 2, only the MCM method indicates good energy focusing at the correct origin time. The envelope, STA/LTA and kurtosis methods fail to suppress the interfering energy from event 1. The kurtosis method exhibits severe oscillation in the stacking functions and the STA/LTA method shows multiple-peaks in the stacking functions, which are detrimental to the correct identification of event 2.

502 **5 INFLUENCE OF VELOCITY MODEL**

503 Our MCM location method is applicable to different velocity models, including anisotropy, as long  
 504 as a sufficiently accurate traveltime table can be built. However in practice, an accurate velocity  
 505 model is not always possible to obtain. Typically an inaccurate velocity structure may cause large  
 506 deviation in source location (Usher et al. 2013). The deviation in source location will lead to an  
 507 accumulated error in the source mechanism determination and make source mechanism character-  
 508 ization difficult (Grigoli et al. 2016). In this section, we will discuss the influence of uncertainties  
 509 in velocity model on source location.

510 In order to test the influence of the velocity model on source location, we use three different  
 511 velocity models to generate the travelttime table for migration. One is the true layered velocity  
 512 model, which will produce the correct travelttime table for the P- and S-waves. The other two are  
 513 homogeneous velocity models, representing the simplest possible models. For the two homoge-  
 514 neous models, the first is obtained by calculating the root-mean-square (RMS) velocity of the top  
 515 three layers, and leads to a model with velocity too fast for calculating the correct travelttime table  
 516 compared with the true velocity model. Using a high velocity model, the arrival times of the P-  
 517 and S-waves are shifted earlier. The second homogeneous model is relatively slow compared to the  
 518 real model, which will delay the arrival times of the P- and S-waves. The P- and S-wave velocities  
 519 of the high velocity model are 3.7984 km/s and 2.0437 km/s, respectively, which are the RMS ve-  
 520 locities of the true model. The P- and S-wave velocities of the low velocity model are 3.362 km/s  
 521 and 1.772 km/s, respectively, which are the arithmetic mean velocities of the first two layers of the  
 522 true model. These two velocity models have different Vp/Vs ratios which adds a further element  
 523 of variability.

524 If a homogeneous model instead of a true layered model is used in the migration, the migration  
 525 results will tend to have deviations in vertical direction (Figs 18-19) because the receivers are at  
 526 the surface. The location deviations depend on the amount of over/under prediction of the true  
 527 velocity model. Here the recording array is symmetrical about the epicenter, thus the event is  
 528 well constrained in the horizontal direction. If the array were not symmetrical about the epicenter,  
 529 horizontal deviations in location would also be expected. The different migration methods exhibit

530 different patterns in the imaging results (as shown in Figs 18-19). The kurtosis and MCM methods  
 531 have higher resolution compared to the envelope and STA/LTA methods. For all four methods, if an  
 532 inaccurate velocity model is used, there will be energy focused at both shallower and larger depth  
 533 than the true source location. The inaccurate velocity model singularizes the trade-off between  
 534 location depth and estimated origin time for surface array. In the shallower part, the energy tends  
 535 to focus at a later time compared to the true origin time of the event, while in the deeper part,  
 536 the energy tends to focus earlier. The location results using different velocity models are shown in  
 537 Table 2. If a low velocity model is used (Fig. 18), the located event is deeper than the true source  
 538 location (except STA/LTA method). While if a high velocity model is used (Fig. 19), the located  
 539 event is shallower than the true source location (except envelope method). The unusual behaviour  
 540 of STA/LTA and envelope methods probably comes from the relatively low resolution in source  
 541 location and more severe trade-off between location depth and estimated origin time for the two  
 542 methods (see Figs 18 and 19). The location results of the MCM and kurtosis methods in the high  
 543 velocity model only have a deviation of a single grid point (50 m). Here, because the RMS velocity  
 544 is used to construct the high velocity model, location results in the high velocity model are better  
 545 (except for STA/LTA). Compared with other methods, the MCM and kurtosis methods are less  
 546 sensitive to the velocity model (especially when overpredicting the model velocities) and have  
 547 higher imaging resolution.

## 548 6 SOURCE LOCATION IN COMPLEX MODELS

549 Subsurface heterogeneity can affect the recorded waveforms at different stations. In order to test  
 550 the performance of our MCM method in the presence of strong heterogeneity, we compare the lo-  
 551 cation performance of the MCM with other migration-based methods on a complex 3D overthrust  
 552 model (Aminzadeh et al. 1997). The P-wave velocity of the overthrust model are shown in Figs  
 553 20 and 21, which are widely used to test and verify various geophysical algorithms (Virieux &  
 554 Operto 2009; Yuan et al. 2015; Shi et al. 2018a). The adopted overthrust model has a size of 4 km  
 555 × 4 km × 0.93 km in the X, Y and Z directions. As shown in Fig. 21, the overthrust model shows  
 556 many complex structures including numerous thrust faults and fluvial deposits, which allows us to

study the influence of heterogeneity on waveform coherency and source location. Full wavefields for this model are generated using the finite difference modeling technique of Shi et al. (2018a). A vertical strike-slip source is placed in the middle of the model, which has coordinates of (1.995, 1.995, 0.46) km in the X, Y and Z directions (Fig. 21). A Ricker wavelet with a peak frequency  $f_m$  of 40 Hz and a time delay of  $1.1/f_m$  is used as the source time function in the simulation.

A monitoring array consisting of 100 receivers ( $10 \times 10$  receiver lines at an average horizontal interval of 400 m and at depth of 150 m) is used to record the three component particle velocities with a sampling rate of 5000 samples/s in the simulation (Fig. 20). The receivers lie in different geological units and the geological structures beneath the receivers are also different. The thicknesses of most layers in the overthrust model are about 15 - 90 m, which are comparable to the average wavelengths of P-wave (100 m) and S-wave (59 m). Therefore, due to complex structures of the model and the velocity heterogeneity, scattering is strong in the simulation. As can be seen in the record section shown in Fig. 22, the recorded wavefields are very complex with strong evidence of scattering and coda waves. Because of the strong 3D heterogeneity and complex structures of the model, the calculated arrival times of the direct P- and S-waves are not smooth (Fig. 22).

Waveform migration is performed on 102400 potential source positions ( $80 \times 80 \times 16$  in the X, Y and Z directions respectively) with 50 m interval. Origin times from -0.3 s to 0.3 s with an interval of 1 ms are scanned. In practice, it is almost impossible to obtain an exact velocity model. Therefore waveform migrations are conducted on a smoothed velocity model which is obtained by using a box convolution kernel with a size of 21 grid points (Figs 20 and 21). Fig. 23 shows the migration results using the smoothed velocity model for the four methods, i.e. envelope, STA/LTA, Kurtosis migration and the MCM. The black ball shows the correct source position. Apart from the envelope migration, the other three methods can all correctly locate the source position. MCM and STA/LTA migration perform the best. Kurtosis migration has relatively higher imaging resolution. However the stacking results of kurtosis migration exhibit much more oscillations than the other results, which might come from interferences of the scattering waves and multiples. Therefore compared to the other three methods, kurtosis migration tend to be more unstable. Because of the influence of scattering waves and model heterogeneity, waveform coherency between different

stations decreases. The stacked waveform coherency at the correct source location is 0.64. The decreased waveform coherency will weaken the noise resistance of the MCM method, however MCM can still obtain stable and accurate location results if the coherency of recorded waveforms are not completely destroyed by the model heterogeneity or noise. Therefore MCM can be applied to complex models where scattering and coda waves are generated and obtain reliable and accurate location results using a smoothed version of the complex velocity model.

## 7 DISCUSSION

The calculation of multichannel coherency also brings extra computations for the MCM method. With precalculated characteristic functions, the calculation of conventional migration-based method is proportional to  $N_s * N_t * N$  ( $N_s$  is the number of image points,  $N_t$  is the number of searching origin time points,  $N$  is the number of stations). With the two channel-based coherency (equation (3)), the calculation of the MCM method is proportional to  $N_s * N_t * (N * (N - 1)/2) * 10M_t$  ( $M_t$  is the length of the coherency analysis time window). Compared with conventional migration method, the calculation burden of the MCM method is increased greatly. However, the MCM location method can be implemented quite efficiently. At every imaging point, the calculation of the correlation coefficient matrix (equation (10)) and the stacking coherency (equation (11)) are independent of all other imaging points. The coherency calculation is also independent of the various origin times. Thus the whole calculation of the MCM method is highly parallelizable on distributed computing architectures. Specifically, the MCM location algorithm can be parallelized on a large scale according to image points and/or origin times using graphics processing unit (GPU). Implementation of a parallelized MCM location algorithm over a large amount of calculation nodes or GPUs would make the method a suitable real time monitoring method.

For MCM using surface arrays, the horizontal resolution of the imaging results is higher than the vertical resolution (Fig. 10) and this is due to the adopted time window in the coherency analysis. When moving the image point slightly in the vertical direction from the true source location, the arrival times of the P- and S-phases for all the traces will increase or decrease simultaneously. However, due to the use of a coherency analysis window, the P- and/or S-phases arrivals can still

612 be incorporated into the time window of the coherency analysis, which contributes to a high coher-  
613 ence value. When moving the image point slightly in the horizontal direction from the true source  
614 location, the arrival times for different traces will increase or decrease differently according to the  
615 relative position of the source and receivers. Thus only a small part of P- and/or S-phases arrivals in  
616 the received data will fall into the coherency analysis window. Thus the stacking of the coherence  
617 value decreases more rapidly in the horizontal direction than in the vertical direction. Thus the  
618 sensitivity of the stacking function in the horizontal direction contributes to the higher horizontal  
619 resolution. It is feasible to increase the imaging resolution by using a smaller coherency analy-  
620 sis window. However, a smaller time window is detrimental for noise suppression. In practice, an  
621 optimum trade-off between the imaging resolution and noise suppression is required. Adaptively  
622 adjusting the coherency analysis window according to the noise level of the data could be a good  
623 way to give consideration to the imaging resolution and noise suppression.

624 For the envelope and STA/LTA migration, large deviations in the vertical direction are often  
625 observed especially when the adopted velocity model for migration is inaccurate (as shown in Figs  
626 18 and 19). The characteristic functions of the envelope and STA/LTA migration cannot accurately  
627 identify the arrival of P- and S-waves. The local maximum values in the characteristic functions  
628 of the envelope and STA/LTA methods often appears slightly later than the exact arrival times of  
629 direct P- and S-waves. Due to the inaccurate estimation of the arrival times of direct P- and S-  
630 waves, the envelope and STA/LTA migration suffer more severe trade-off between location depth  
631 and estimated event origin time compared with other methods. The spatial imaging resolution of  
632 the envelope and STA/LTA methods is lower compared to the MCM and kurtosis method. For  
633 conventional migration-based location methods, the spatial and temporal imaging resolution is re-  
634 lated to the local shape of the characteristic functions nearby the arrivals of direct P- and S-waves.  
635 The sharper the characteristic function, the higher the imaging resolution. A wide waveform band-  
636 width in characteristic functions nearby the arrivals of direct P- and S-waves will make it hard  
637 to distinguish the traveltime difference between adjacent image points. The characteristic func-  
638 tions of the envelope and STA/LTA method have a wide waveform bandwidth nearby the direct  
639 P- and S-wave arrivals, thus lead to a relatively low imaging resolution. The waveform bandwidth

nearby the direct P- and S-wave in the characteristic function arrivals can be used to estimate the location uncertainties in the migration-based location method. In contrast, due to the application of derivatives in the kurtosis migration method (Langet et al. 2014), the characteristic function shows more accurate representation for the arrival times of direct P- and S-waves and has a narrower waveform bandwidth nearby the direct P- and S-wave arrivals. Thus for the kurtosis method, the location depth has less uncertainties and trade-off with estimated origin time, and the imaging resolution is higher compared to envelope and STA/LTA methods. MCM is applied directly to original seismic waveforms, and the stacked pairwise waveform coherency decreases rapidly when imaging points deviate from the true source location. Therefore, MCM has high imaging resolution and less location uncertainty compared to conventional migration methods.

In the MCM method, the length of coherency analysis time window is the only parameter that need to be adjusted. Because the imaging result of the MCM method is not very sensitive to the length of the coherency analysis time window, the time window length can be easily determined according to the length of the source time function, frequency band of the data and noise level. Normally the noise level is the major factor that influences the choice of time window. In contrast, the STA/LTA and kurtosis methods have several parameters to adjust, such as time window and frequency band. The migration performance is often highly depend on the choice of these parameters. In practice, it is difficult to obtain a set of optimum parameters that are suitable for all seismic events in the dataset.

In practice, seismic data recorded by local stations might be contaminated by coherent noise such as injection noise and meteorological noise (Birnie et al. 2016). This coherent noise can form severe challenges for migration-based location methods as the coherent noise may be continuous in space and time (Shi et al. 2018b). In these cases, additional measures such as automatic quality control are needed to obtain a stable and reliable location results (Shi et al. 2018b). In addition, scattering together with medium heterogeneity can degrade the waveform coherency, and thus affect the location performance of MCM. However as long as the waveform coherency among stations are not completely undermined by heterogeneity of the subsurface, the MCM method could still achieve a reliable and accurate location result. In the situation of severe decorrelation

668 because of heterogeneity, measures e.g. deconvoluting with empirical Green's functions to remove  
669 the effects of media heterogeneity and recover waveform coherency among receivers can help  
670 improve the location performance for MCM.

671 Compared to downhole arrays, surface arrays used in microseismic monitoring often have  
672 larger recording aperture and have a large station density, which are particularly conducive to the  
673 migration-based location methods. Through utilizing the coherency of waveforms, the migration-  
674 based location method can resist noise and obtain a high quality imaging result. By calculating the  
675 pairwise coherency of the recorded waveform data, our MCM method further extends the avail-  
676 able information used for migration and obtains better imaging resolution and noise resistance.  
677 Compared with downhole array, a surface array of microseismic monitoring has much better hori-  
678 zontal imaging resolution but shows high uncertainties in depth location due to the trade-off with  
679 the estimated origin time. Whereas downhole arrays are better at depth location, but have poor  
680 horizontal imaging resolution. Migration using a combination of surface and downhole array data  
681 might contribute to a better imaging result both in the vertical and horizontal directions.

## 682 8 CONCLUSIONS

683 In this paper we have proposed a novel migration-based method for locating seismic sources. This  
684 new method utilizes the coherency among traces and greatly expands the available information  
685 used for source location. The MCM location method provides an automated seismic location tool,  
686 which is suitable for dealing with large data volume or abundant seismic events. The computational  
687 cost of the MCM method does not depend on the number of seismic events, yet is dependant on  
688 the recording times and the number of imaging grid points. As the MCM is highly parallelizable,  
689 it has the potential to be developed as a real-time location method for natural or induced seismic  
690 monitoring. We have shown that the MCM has the ability to resist strong random noise, where the  
691 random noise analysis has exhibited excellent imaging performance for the MCM method in the  
692 presence of strong noise. Compared to other methods, the location results of the MCM have higher  
693 resolution and are more stable. Robustness tests with an extremely weak event have shown that  
694 the MCM can suppress strong interference and obtain a robust imaging result. The MCM method

695 can still achieve a better imaging result compared to other methods when using incorrect velocity  
 696 models for the migration. This new method is very suitable for locating local seismic events with  
 697 dense monitoring networks, where the waveform coherency is generally preserved.

## 698 ACKNOWLEDGMENTS

699 We would like to thank the editors and reviewers for constructive comments. P. Shi is funded  
 700 by a China Scholarship Council/University of Leeds scholarship. A. Nowacki is supported by a  
 701 Leverhulme Early Career Fellowship.

## 702 REFERENCES

- 703 Allen, R., 1982. Automatic phase pickers: Their present use and future prospects, *Bull. Seismol. Soc. Am.*,  
 704 **72**(6B), S225–S242.
- 705 Aminzadeh, F., Jean, B., & Kunz, T., 1997. *3-D salt and overthrust models*, Society of Exploration Geo-  
 706 physicists.
- 707 Arfken, G. B. & Weber, H. J., 1999. Mathematical methods for physicists.
- 708 Artman, B., Podladtchikov, I., & Witten, B., 2010. Source location using time-reverse imaging, *Geophys.  
 Prospect.*, **58**(5), 861–873.
- 710 Bai, C.-y. & Kennett, B., 2000. Automatic phase-detection and identification by full use of a single three-  
 711 component broadband seismogram, *Bull. Seismol. Soc. Am.*, **90**(1), 187–198.
- 712 Birnie, C., Chambers, K., Angus, D., & Stork, A. L., 2016. Analysis and models of pre-injection surface  
 713 seismic array noise recorded at the aquistore carbon storage site, *Geophys. J. Int.*, **206**(2), 1246–1260.
- 714 Cesca, S. & Grigoli, F., 2015. Chapter two-full waveform seismological advances for microseismic mon-  
 715 itoring, *Adv. Geophys.*, **56**, 169–228.
- 716 Drew, J., White, R. S., Tilmann, F., & Tarasewicz, J., 2013. Coalescence microseismic mapping, *Geophys.  
 J. Int.*, **195**(3), 1773–1785.
- 718 Ezekiel, M. & Fox, K. A., 1959. Methods of correlation and regression analysis: linear and curvilinear.
- 719 Fink, M., Cassereau, D., Derode, A., Prada, C., Roux, P., Tanter, M., Thomas, J.-L., & Wu, F., 2000.  
 720 Time-reversed acoustics, *Rep. Prog. Phys.*, **63**(12), 1933.
- 721 Gharti, H. N., Oye, V., Roth, M., & Kühn, D., 2010. Automated microearthquake location using envelope  
 722 stacking and robust global optimization, *Geophysics*, **75**(4), MA27–MA46.
- 723 Grigoli, F., Cesca, S., Amoroso, O., Emolo, A., Zollo, A., & Dahm, T., 2013a. Automated seismic event  
 724 location by waveform coherence analysis, *Geophys. J. Int.*, **196**(3), 1742–1753.

- 725 Grigoli, F., Cesca, S., Vassallo, M., & Dahm, T., 2013b. Automated seismic event location by travel-time  
726 stacking: An application to mining induced seismicity, *Seismol. Res. Lett.*, **84**(4), 666–677.
- 727 Grigoli, F., Cesca, S., Krieger, L., Kriegerowski, M., Gammaldi, S., Horalek, J., Priolo, E., & Dahm, T.,  
728 2016. Automated microseismic event location using master-event waveform stacking, *Sci. Rep.*, **6**, 25744.
- 729 Halliday, D. & Curtis, A., 2008. Seismic interferometry, surface waves and source distribution, *Geophys.*  
730 *J. Int.*, **175**(3), 1067–1087.
- 731 Kaderli, J., McChesney, M. D., & Minkoff, S. E., 2015. Microseismic event estimation in noisy data via  
732 full waveform inversion, in *SEG Technical Program Expanded Abstracts 2015*, pp. 1159–1164, Society  
733 of Exploration Geophysicists.
- 734 Kao, H. & Shan, S.-J., 2004. The source-scanning algorithm: Mapping the distribution of seismic sources  
735 in time and space, *Geophys. J. Int.*, **157**(2), 589–594.
- 736 Kao, H. & Shan, S.-J., 2007. Rapid identification of earthquake rupture plane using source-scanning  
737 algorithm, *Geophys. J. Int.*, **168**(3), 1011–1020.
- 738 Langet, N., Maggi, A., Michelini, A., & Brenguier, F., 2014. Continuous kurtosis-based migration for  
739 seismic event detection and location, with application to piton de la fournaise volcano, la réunion, *Bull.*  
740 *Seismol. Soc. Am.*, **104**(1), 229–246.
- 741 Larmat, C., Montagner, J.-P., Fink, M., Capdeville, Y., Tourin, A., & Clévédé, E., 2006. Time-reversal  
742 imaging of seismic sources and application to the great sumatra earthquake, *Geophys. Res. Lett.*, **33**(19).
- 743 Larmat, C., Guyer, R., & Johnson, P., 2009. Tremor source location using time reversal: Selecting the  
744 appropriate imaging field, *Geophys. Res. Lett.*, **36**(22).
- 745 Liao, Y.-C., Kao, H., Rosenberger, A., Hsu, S.-K., & Huang, B.-S., 2012. Delineating complex spatiotem-  
746 poral distribution of earthquake aftershocks: An improved source-scanning algorithm, *Geophys. J. Int.*,  
747 **189**(3), 1753–1770.
- 748 McMechan, G. A., 1982. Determination of source parameters by wavefield extrapolation, *Geophys. J. Int.*,  
749 **71**(3), 613–628.
- 750 Podvin, P. & Lecomte, I., 1991. Finite difference computation of traveltimes in very contrasted velocity  
751 models: a massively parallel approach and its associated tools, *Geophys. J. Int.*, **105**(1), 271–284.
- 752 Ramos-Martínez, J. & McMechan, G. A., 2001. Source-parameter estimation by full waveform inversion  
753 in 3d heterogeneous, viscoelastic, anisotropic media, *Bull. Seismol. Soc. Am.*, **91**(2), 276–291.
- 754 Ruigrok, E., Gibbons, S., & Wapenaar, K., 2016. Cross-correlation beamforming, *J. Seismol.*, pp. 1–14.
- 755 Saragiotis, C. D., Hadjileontiadis, L. J., & Panas, S. M., 2002. Pai-s/k: A robust automatic seismic p phase  
756 arrival identification scheme, *IEEE Trans. Geosci. Remote Sens.*, **40**(6), 1395–1404.
- 757 Shi, P., Angus, D., Nowacki, A., Yuan, S., & Wang, Y., 2018a. Microseismic full waveform modelling in  
758 anisotropic media with moment tensor implementation, *Surv. Geophys.*.
- 759 Shi, P., Nowacki, A., Rost, S., & Angus, D., 2018b. Automated seismic waveform location using Multi-

- channel Coherency Migration (MCM)–II. Application to induced and volcano-tectonic seismicity, *Submitted to Geophys. J. Int.*.
- Steiner, B., Saenger, E. H., & Schmalholz, S. M., 2008. Time reverse modeling of low-frequency microtremors: Application to hydrocarbon reservoir localization, *Geophys. Res. Lett.*, **35**(3).
- Tarantola, A., 1984. Inversion of seismic reflection data in the acoustic approximation, *Geophysics*, **49**(8), 1259–1266.
- Usher, P., Angus, D., & Verdon, J., 2013. Influence of a velocity model and source frequency on microseismic waveforms: some implications for microseismic locations, *Geophys. Prospect.*, **61**(s1), 334–345.
- VanDecar, J. & Crosson, R., 1990. Determination of teleseismic relative phase arrival times using multi-channel cross-correlation and least squares, *Bull. Seismol. Soc. Am.*, **80**(1), 150–169.
- Virieux, J. & Operto, S., 2009. An overview of full-waveform inversion in exploration geophysics, *Geophysics*, **74**(6), WCC1–WCC26.
- Wang, S., Yuan, S., Yan, B., He, Y., & Sun, W., 2016. Directional complex-valued coherence attributes for discontinuous edge detection, *J. Appl. Geophys.*, **129**, 1–7.
- Wapenaar, K., Van Der Neut, J., Ruigrok, E., Draganov, D., Hunziker, J., Slob, E., Thorbecke, J., & Snieder, R., 2011. Seismic interferometry by crosscorrelation and by multidimensional deconvolution: A systematic comparison, *Geophys. J. Int.*, **185**(3), 1335–1364.
- Wassermann, J. & Ohrnberger, M., 2001. Automatic hypocenter determination of volcano induced seismic transients based on wavefield coherence—an application to the 1998 eruption of mt. merapi, indonesia, *J. Volcanol. Geoth. Res.*, **110**(1), 57–77.
- Wu, Y. & McMechan, G. A., 1996. Elastic full-waveform inversion for earthquake source parameters, *Geophys. J. Int.*, **127**(1), 61–74.
- Yuan, S., Wang, S., Luo, C., & He, Y., 2015. Simultaneous multitrace impedance inversion with transform-domain sparsity promotion, *Geophysics*, **80**(2), R71–R80.
- Yuan, S., Liu, J., Wang, S., Wang, T., & Shi, P., 2018. Seismic waveform classification and first-break picking using convolution neural networks, *IEEE Geosci. Remote Sens. Lett.*, **15**(2), 272–276.
- Zhebel, O. & Eisner, L., 2014. Simultaneous microseismic event localization and source mechanism determination, *Geophysics*, **80**(1), KS1–KS9.

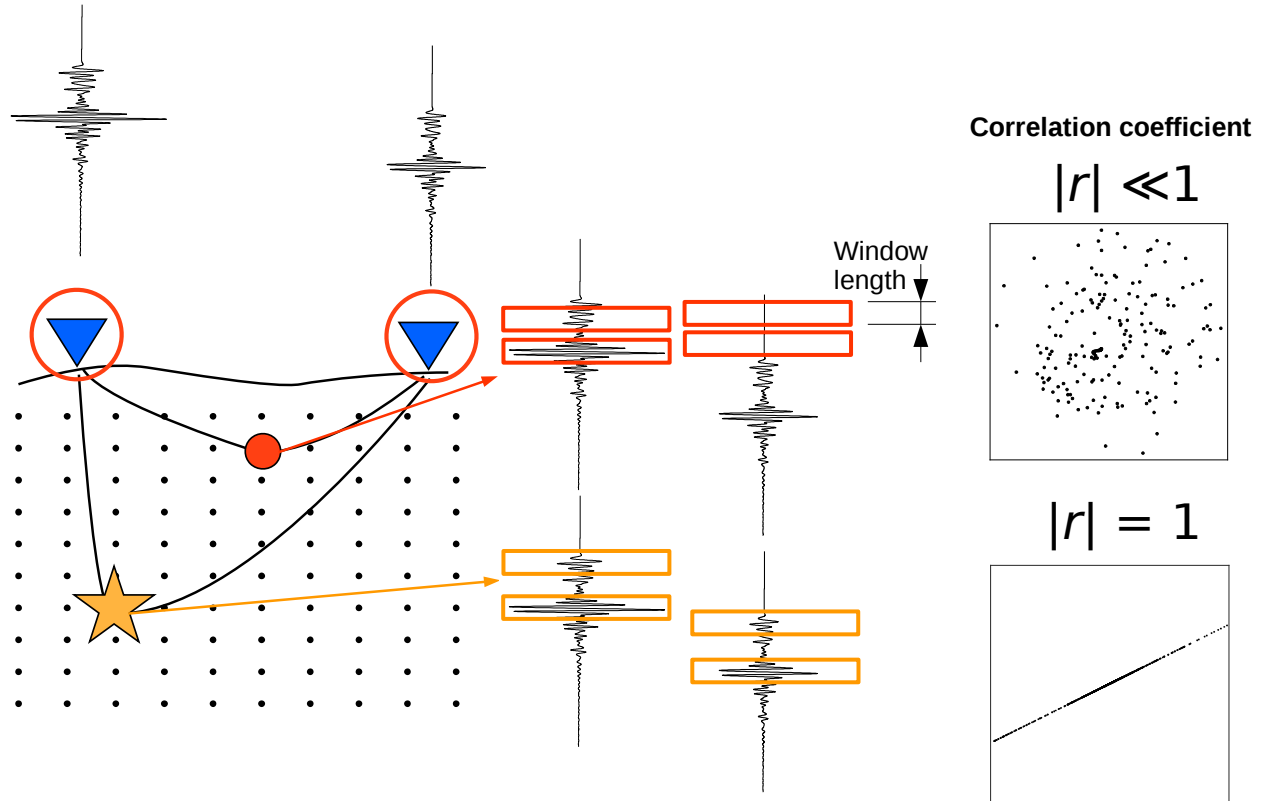


**Figure 1.** Schematic diagram showing the waveform coherency for different imaging points. Black dots show subsurface imaging points. Blue triangles show surface receivers. Orange star represents the true source point which has a high waveform coherency and red circle represents an incorrect imaging point which has a very low waveform coherency.

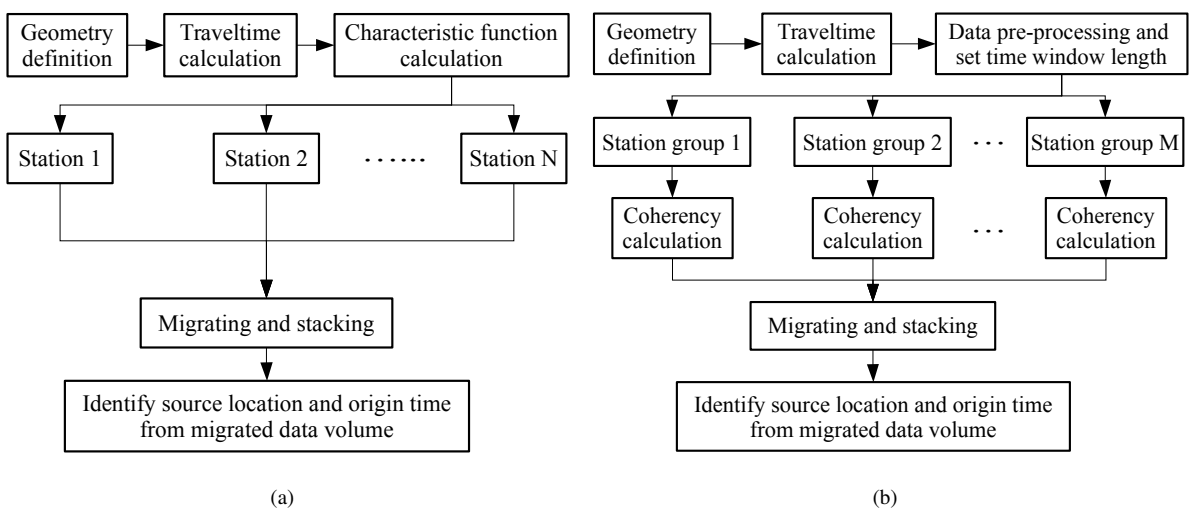
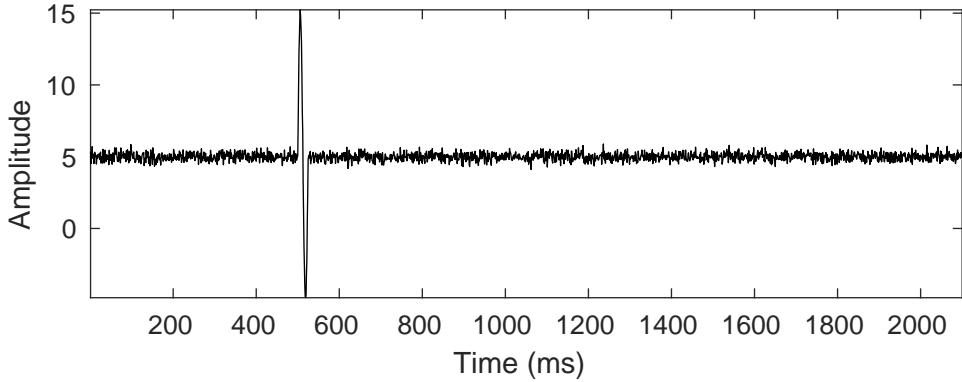
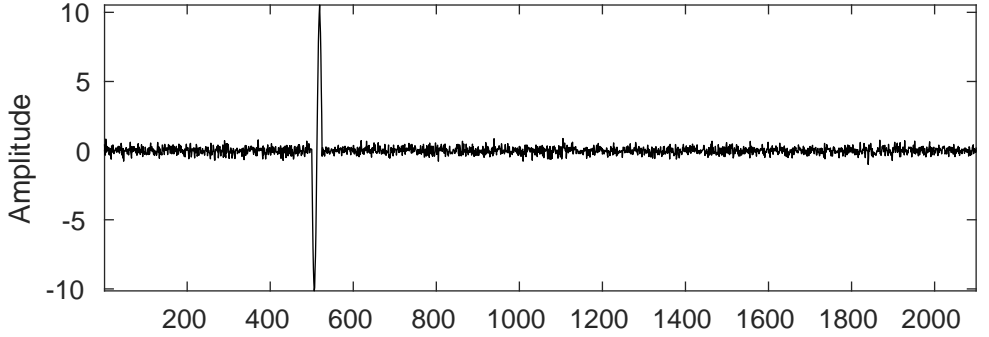
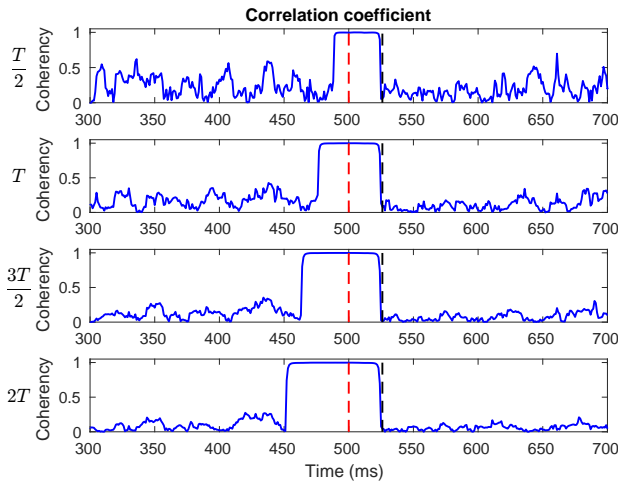


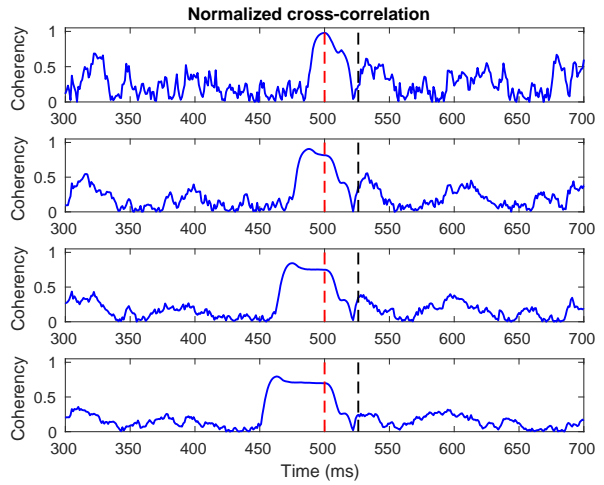
**Figure 2.** (a) Workflow of the traditional migration-based location method. (b) Workflow of the MCM method.



(a)



(b)



(c)

**Figure 3.** Coherency of two sinusoidal signals with random noise obtained by a sliding time window of different size. The period ( $T$ ) of the sinusoidal signal is 25 ms. The top row of figure (b) and (c) shows the case with a time window of 13 ms ( $T/2$ ), the second row with a time window of 25 ms ( $T$ ), the third row with a time window of 38 ms ( $3T/2$ ), the bottom row with a time window of 50 ms ( $2T$ ). The red dashed line exhibits the origin time of the sinusoidal signal at 500 ms. The black dashed line exhibits the end time of the sinusoidal signal at 526 ms. (a) The two sinusoidal signals with random noise. The signal-to-noise ratio is 10. (b) The coherency obtained by the Pearson correlation coefficient method using equation 3. (c) The coherency obtained by normalized cross-correlation method using equation 4.

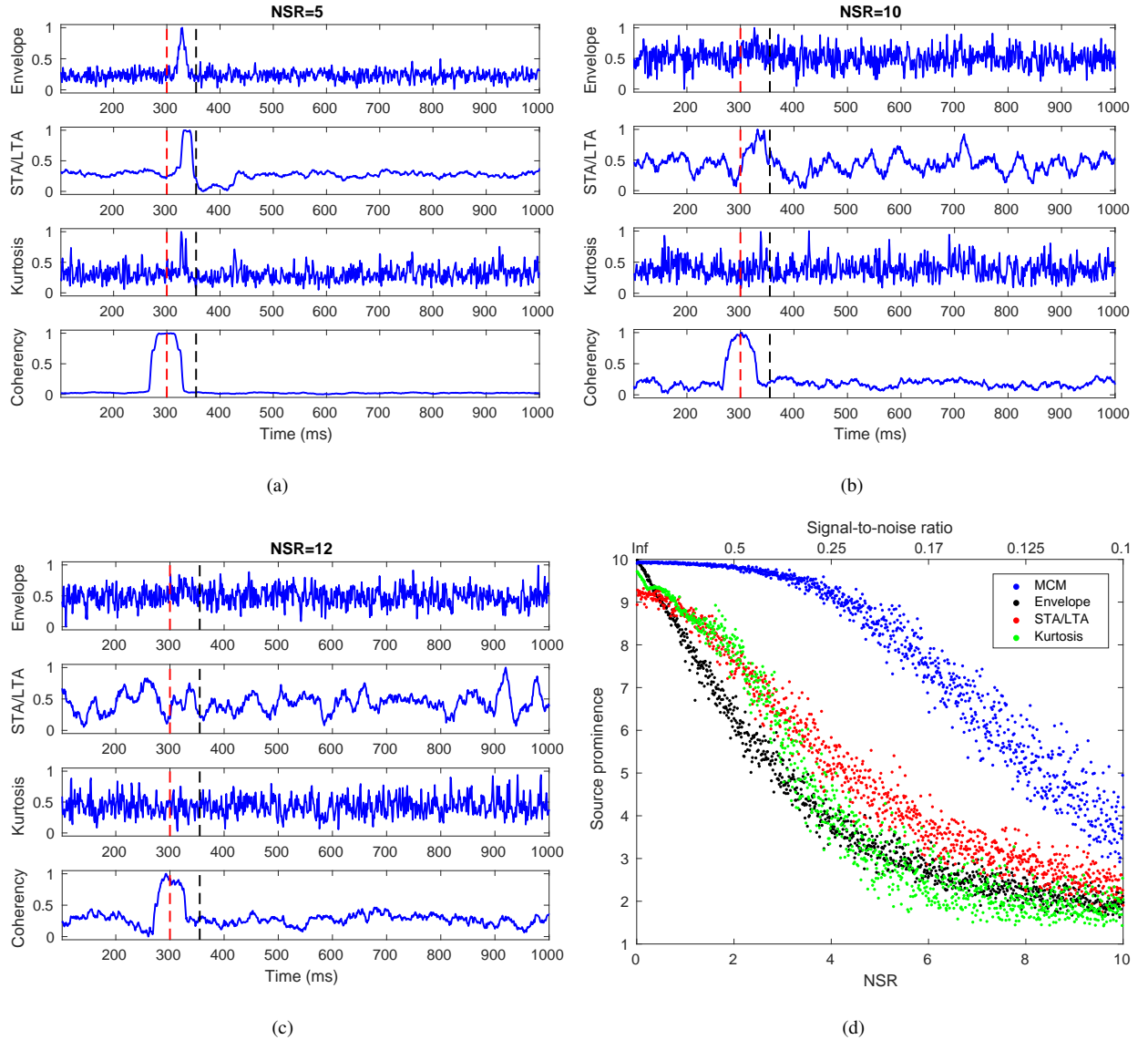


**Figure 4.** Stacking functions and source prominence ( $S_{pro}$ ) at the correct source position under different NSRs for four different migration methods (envelope, STA/LTA, kurtosis and MCM). Total number of available traces is 441. Red and black dashed lines show the origin and end time of the source respectively. The stacking functions for the four different migration methods when NSR is (a) 5, (b) 10, (c) 12. (d) The variation of source prominence with different NSRs. The results are obtained through Monte Carlo simulation with black points showing the envelope method, STA/LTA method (red points), kurtosis method (green points) and MCM method (blue points). Because the stacking energy is not at the same scale for different migration methods, the source prominence is calculated after normalizing the stacking functions between 1 and 10. MCM performs best in the presence of strong random noise.

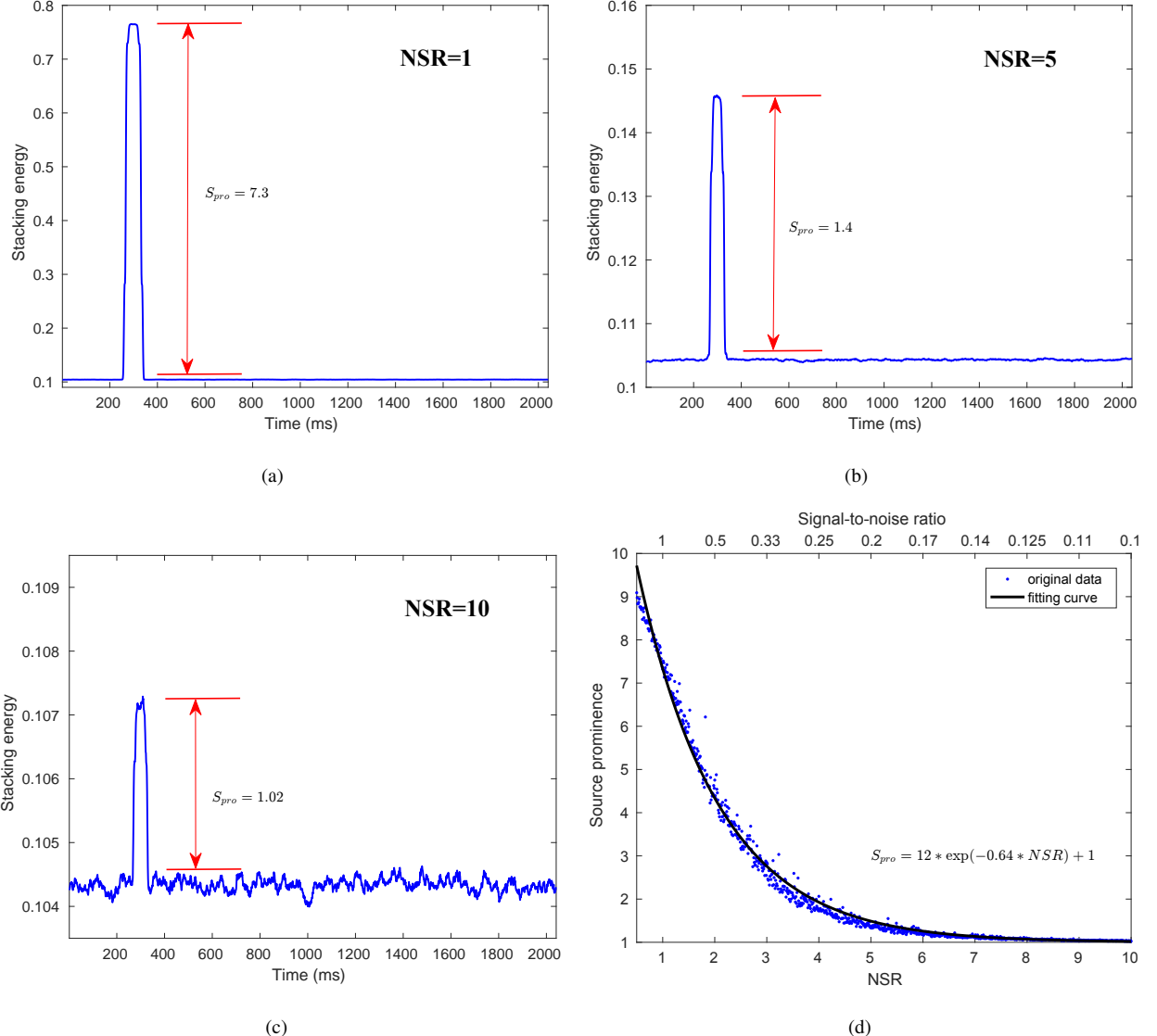


**Figure 5.** Stacking functions at the source position when NSR is (a) 1, (b) 5 and (c) 10 for the MCM method. (d) Variation of source prominence with different NSRs at the source position for the MCM method. Results are obtained through Monte Carlo simulation. Blue points represent the calculated source prominences, and the black line shows the fit to the data. The fitting formula is also shown in the figure. The source prominence is calculated using the simulation results directly without normalization. The total number of available traces is 1000.

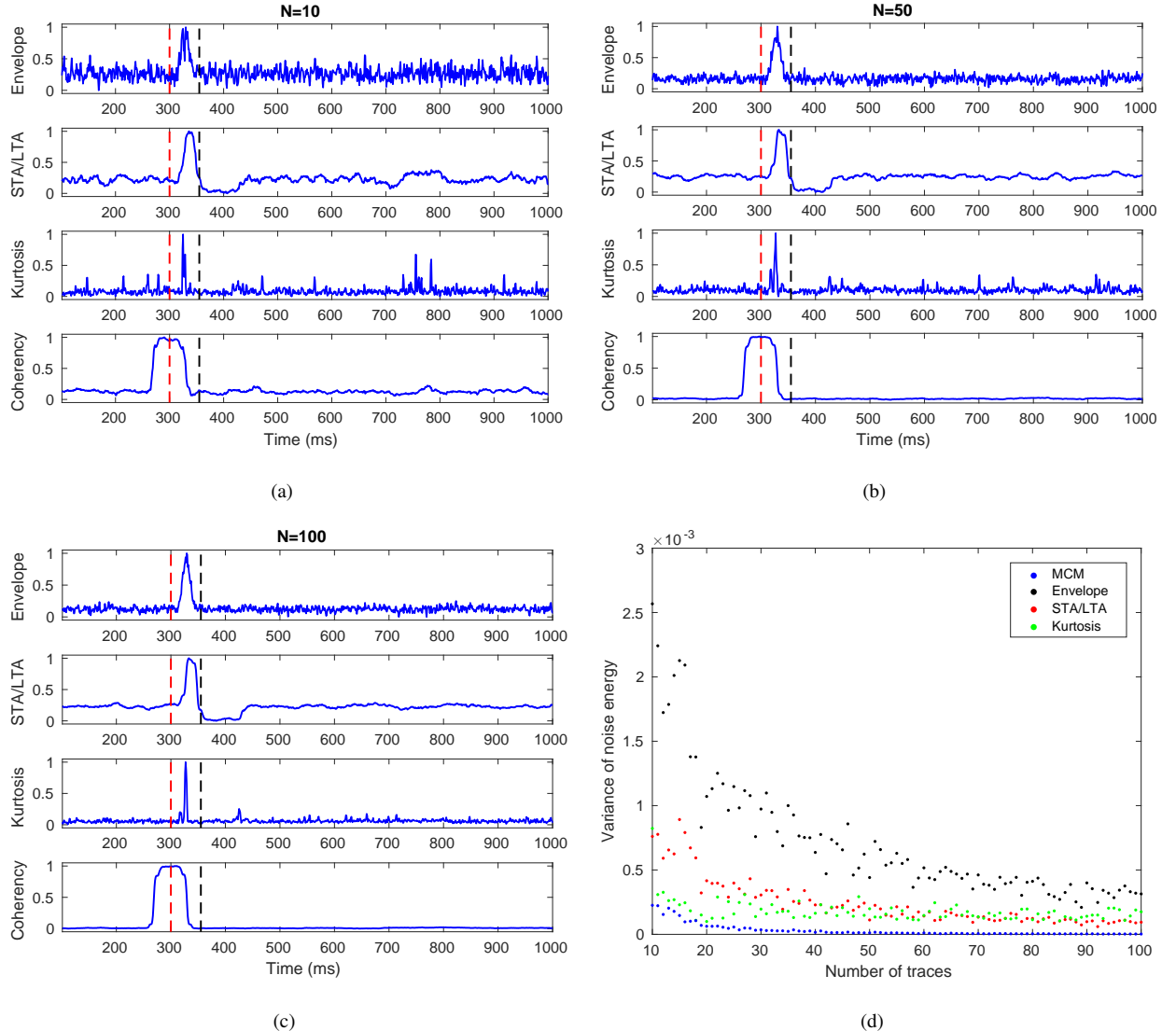


**Figure 6.** Stacking functions and variance of noise energy at the source position under different number of traces ( $N$ ) for the four different migration methods (envelope, STA/LTA, kurtosis and MCM). NSR is 2 for all the figures. Red and black dashed lines show the origin and end time of the source respectively. Stacking functions when  $N$  is (a) 10, (b) 50 and (c) 100. (d) Variation of noise variances with different  $N$ . The results are obtained through Monte Carlo simulation. Black points show the envelope method, red points show STA/LTA method, green points show kurtosis method and blue points show the MCM method. Because the stacking energy is not at the same scale for different migration methods, the source prominence is calculated after normalizing the stacking functions between 0 and 1.

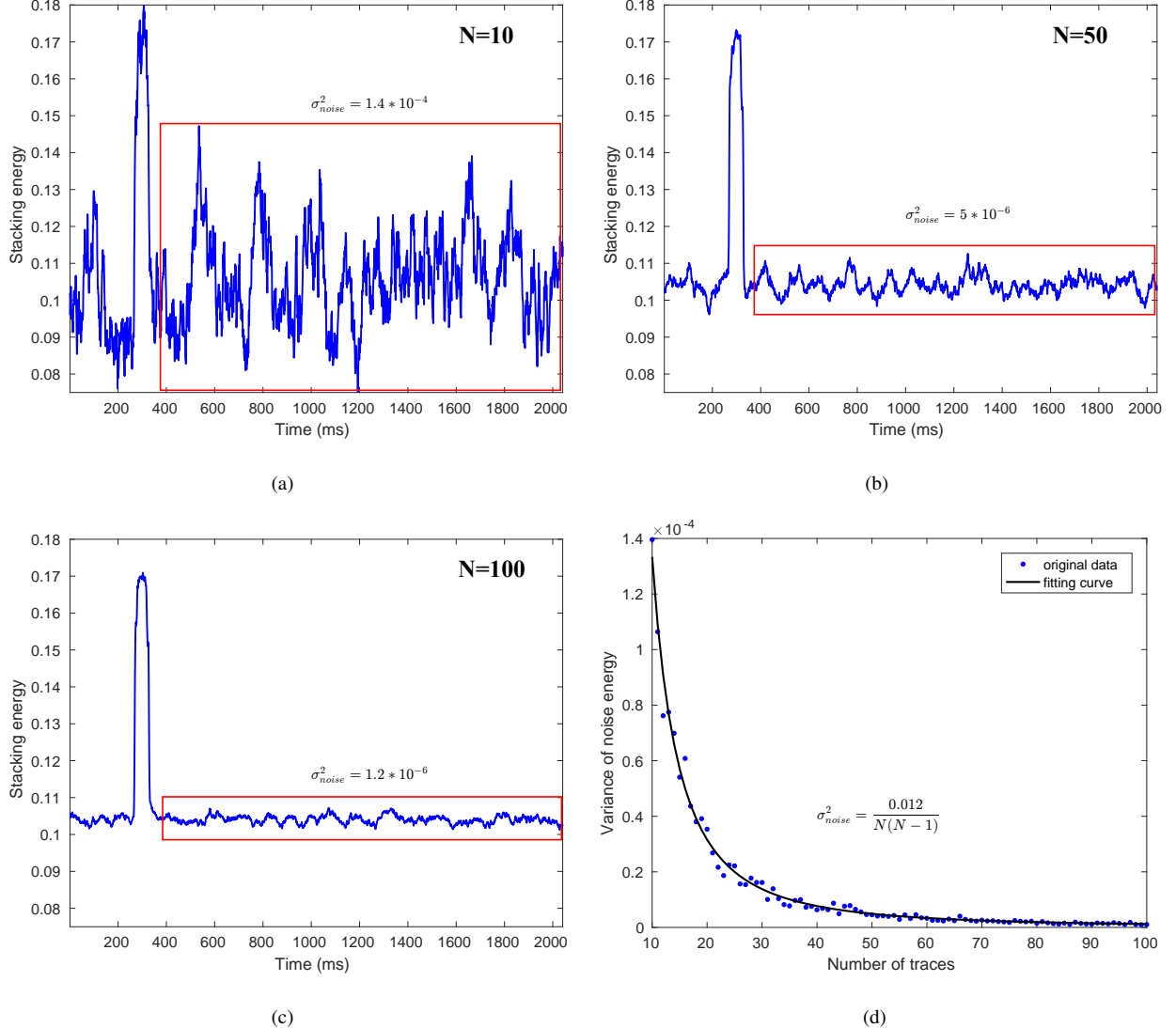


**Figure 7.** Stacking functions at the source position when the trace number ( $N$ ) is (a) 10, (b) 50 and (c) 100 for the MCM method. (d) Variation of the variance of noise energy with different trace numbers at the source position for the MCM method. The results are obtained through Monte Carlo simulation. Blue points represent the calculated variance of noise energy, and the black line shows the fit to the variance data points. The fitting formula is also shown in the figure. The NSR is 4 for all the figures.

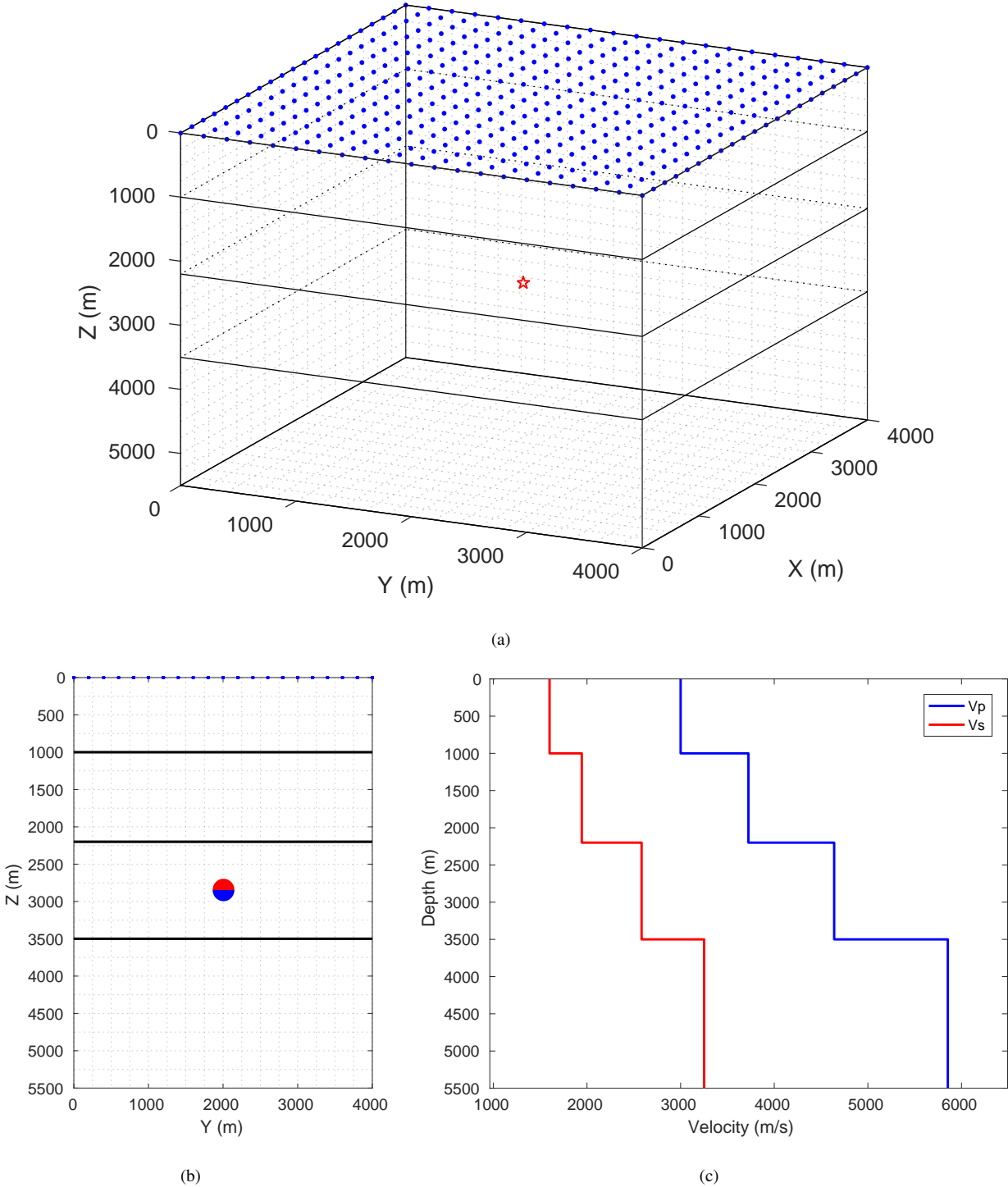


**Figure 8.** The velocity model and receiver geometry for the microseismic monitoring. (a) Layered model showing the velocity and surface array. The red star represents the vertical dip-slip source, blue points represent the surface receivers. 441 receivers are uniformly distributed on the free surface with 21 receiver lines in X direction, 21 receiver lines in Y direction and a lateral interval of 200 m. (b) Vertical profile of the layered model with a beach ball showing the moment tensor source. (c) P- and S-wave velocities used for the migration.

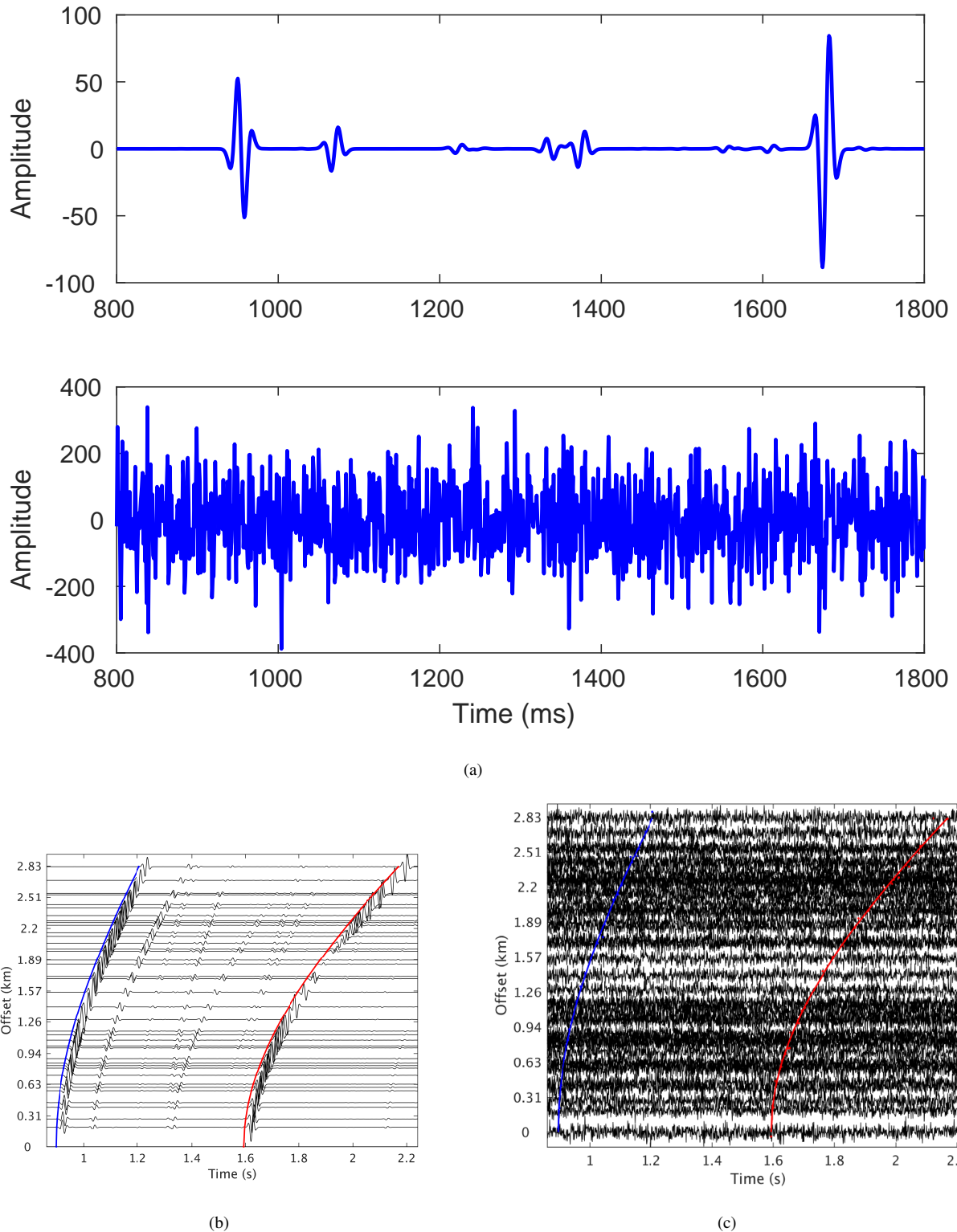


**Figure 9.** The synthetic noise free data (vertical component) and the data after adding noise. The NSR is 6. (a) Synthetic seismogram at trace number 305 (upper) and the same seismogram after adding noise (lower). (b) The record section of the synthetic noise free data. (c) The record section of the noisy data. Blue line shows the arrivals of the direct P-waves. Red line shows the arrivals of the direct S-waves.

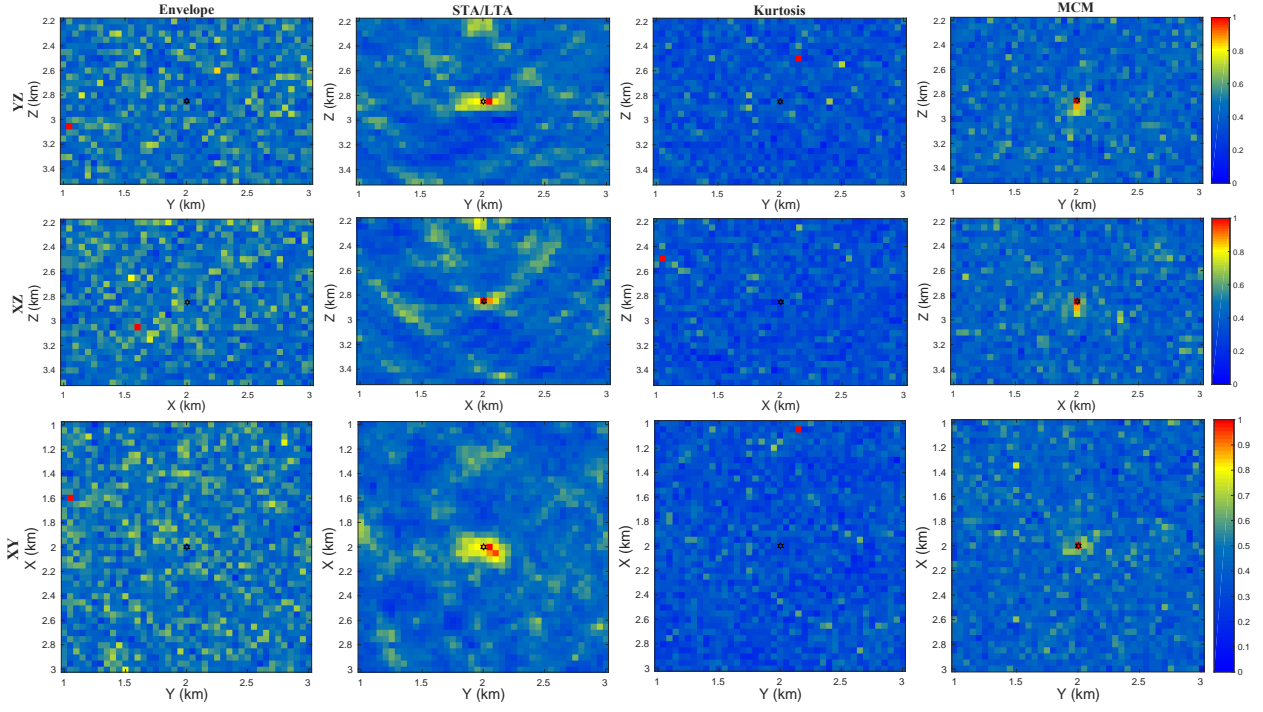


**Figure 10.** Profiles of the migration results through the normalized stacking functions at the stacking maximum for the four migration methods. NSR = 6. For better comparison of different migration results, all the stacking functions have been linearly normalized to the range between 0 and 1. Black hexagrams in the middle of the target area represent the true source location. The first column shows results of envelope, second column for STA/LTA, third column for kurtosis, fourth column for MCM. The first row shows YZ (vertical) profiles, second row shows XZ (vertical) profiles, third row shows XY (horizontal) profiles.

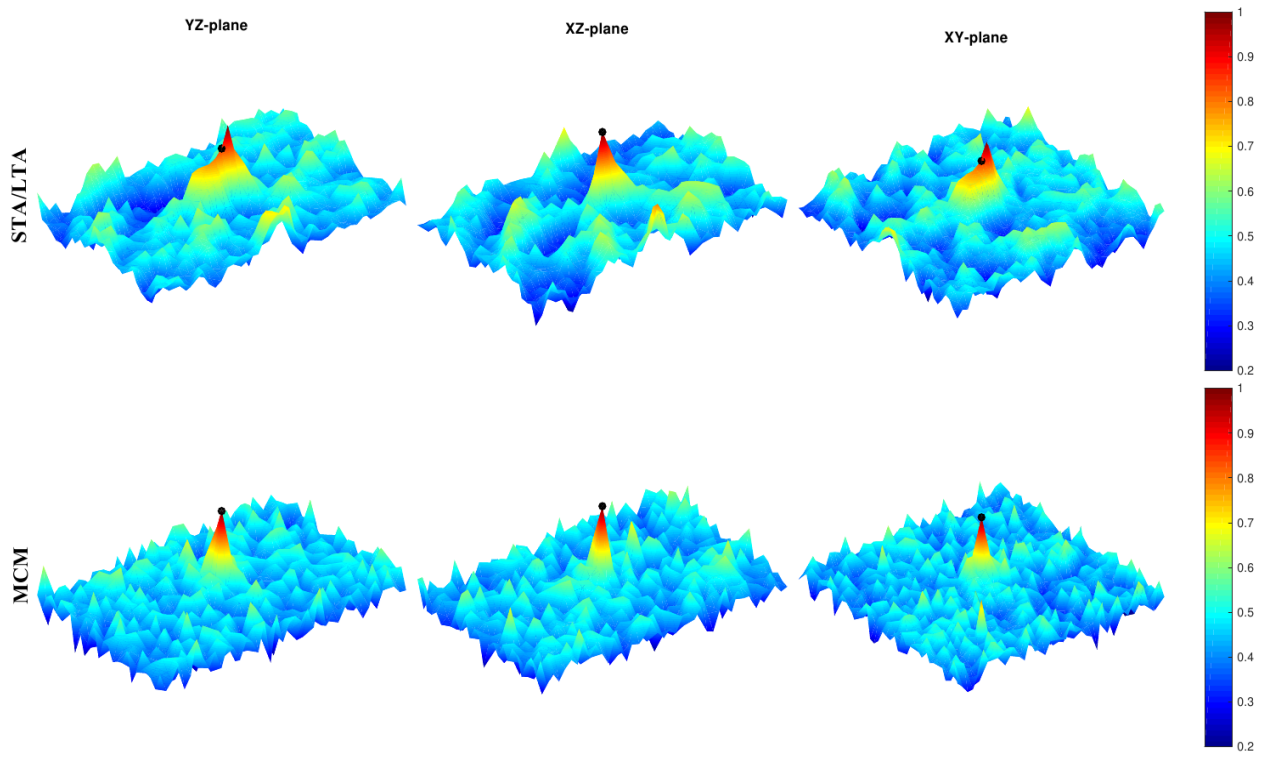


**Figure 11.** 3D profiles of the migration results through the maximum migrated value of normalized stacking functions for the STA/LTA and MCM methods. Black balls show the location of the source event. The first column shows YZ profiles, second column shows XZ profiles, third column shows XY profiles. The first row shows results of the STA/LTA method, second row for MCM.

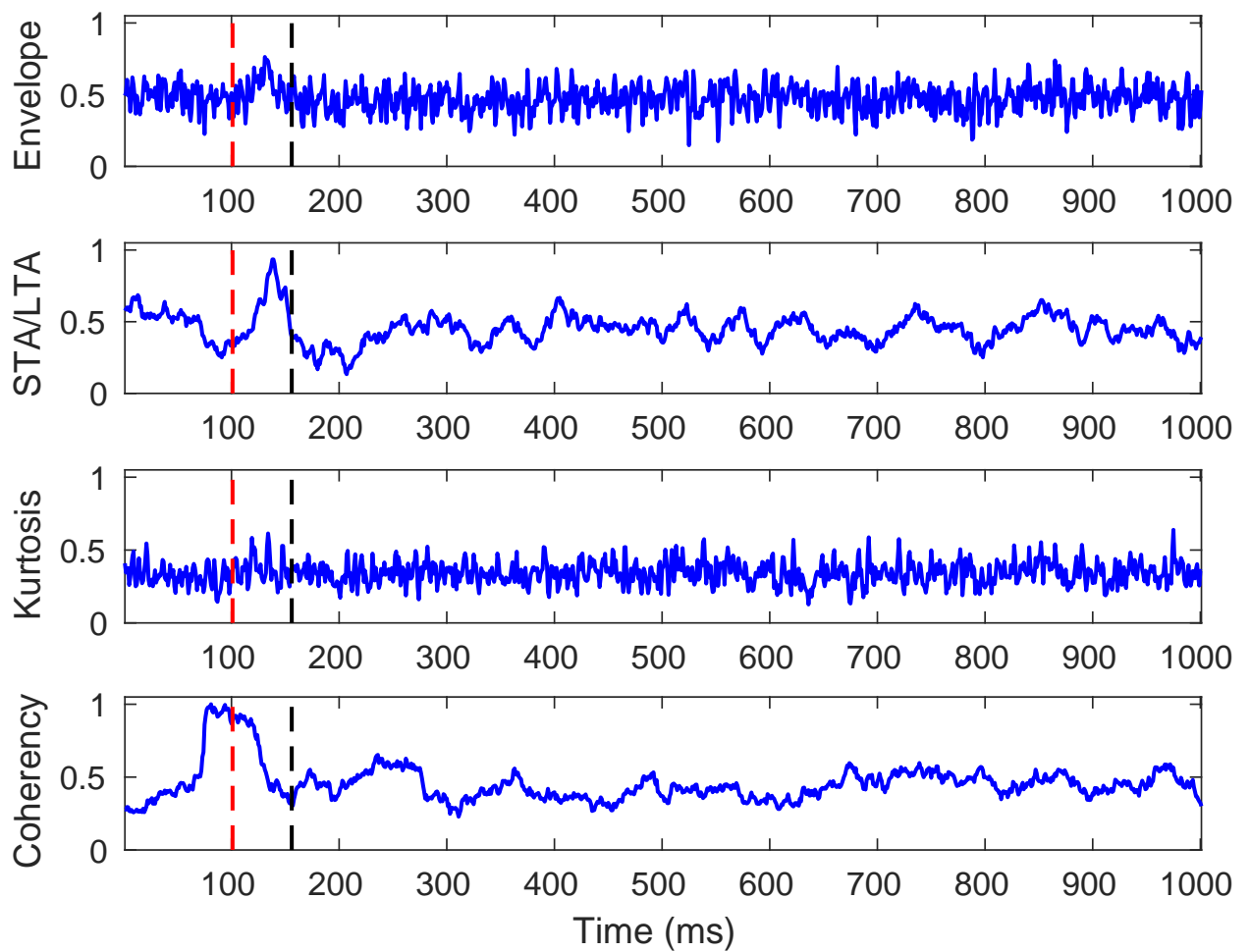


**Figure 12.** The stacking functions at the true source location for the four methods. The red and black dashed line shows the origin time and end time of the source respectively.

**Table 1.** Location results of different methods and comparison with true source location.

	Source location				Location error			
	X (km)	Y (km)	Z (km)	$T_0$ (s)	$\Delta X$ (m)	$\Delta Y$ (m)	$\Delta Z$ (m)	$\Delta T_0$ (s)
True	2.00	2.00	2.85	0.100	-	-	-	-
Envelope	1.60	1.05	3.05	0.565	400	950	200	0.465
STA/LTA	2.00	2.05	2.85	0.136	0	50	0	0.036
Kurtosis	1.05	2.15	2.50	0.199	950	150	350	0.099
Coherency	2.00	2.00	2.85	0.081	0	0	0	-0.019

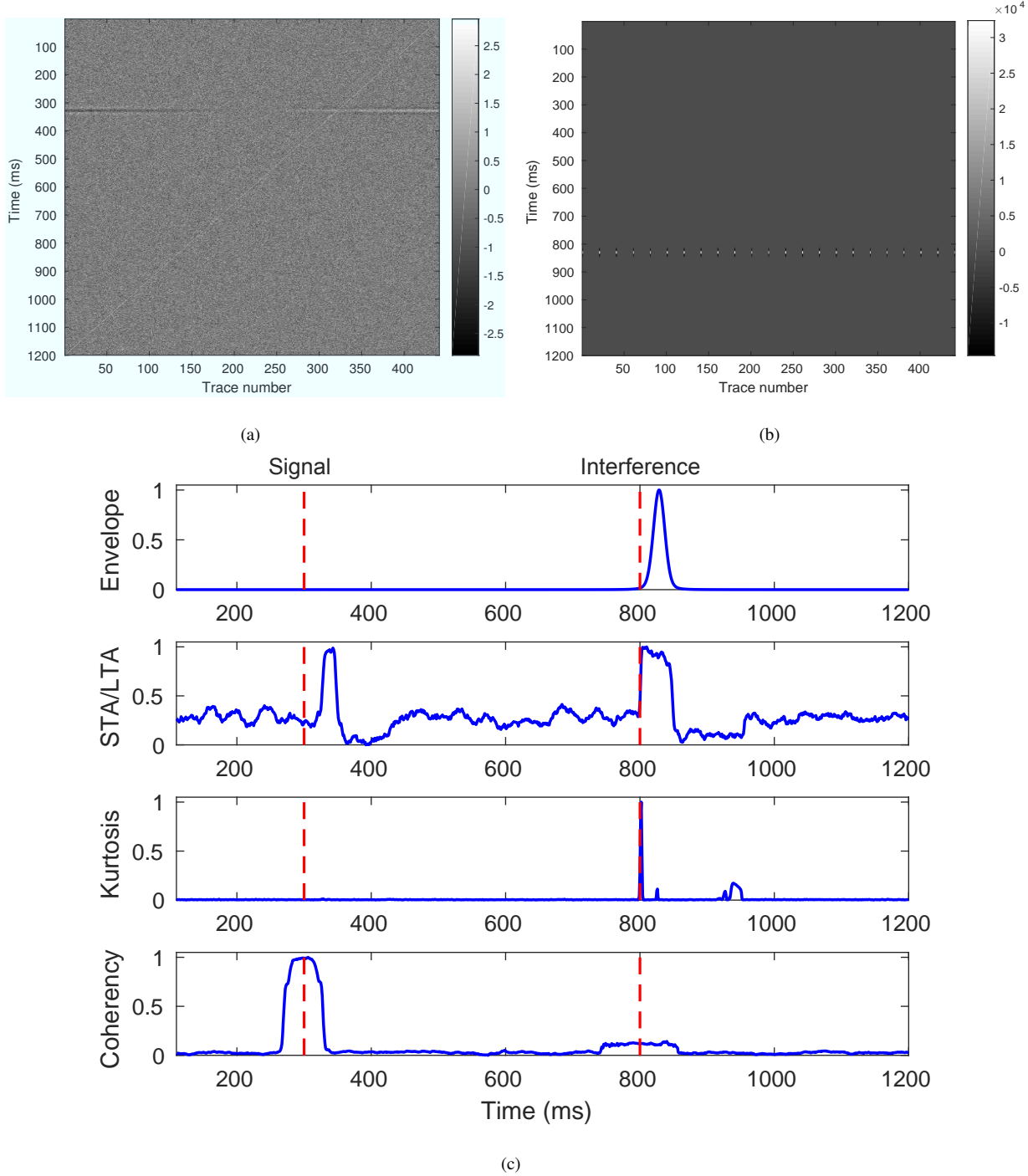
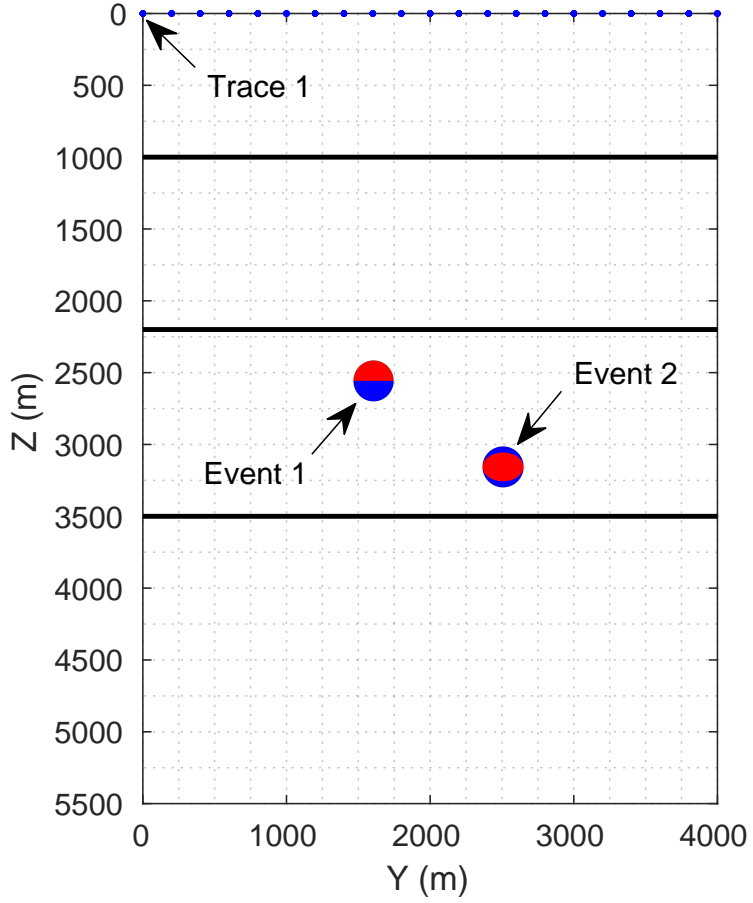
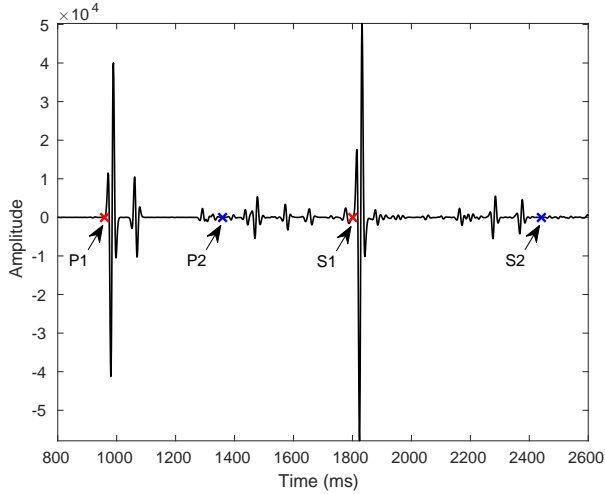


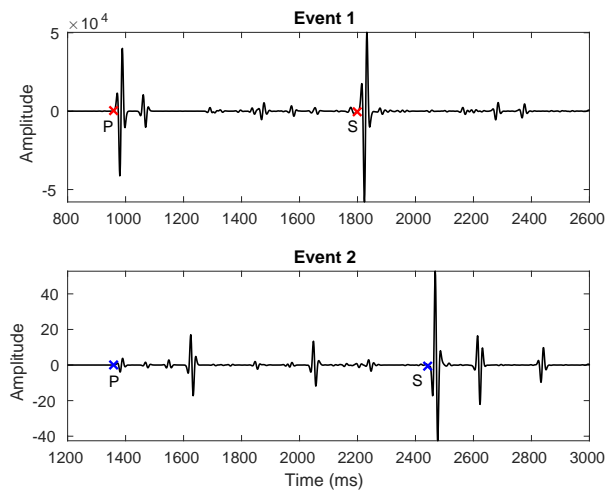
**Figure 13.** (a) The time aligned traces with  $NSR = 3$ . The origin time for the weak signals to be detected is 300 ms. (b) The time aligned traces after adding strong coherent interference signals into 23 of the traces in (a). The amplitude of the interference signals is 32768 times the amplitude of the weak effective signals. The origin time of the interference signals is 800 ms. (c) Stacking functions of the four different methods with red dashed lines showing the origin times of the weak signals and interference signals.



(a)



(b)



(c)

**Figure 14.** (a) Model profile which shows the positions of two events. Event 1 is a vertical dip-slip source and event 2 is a 45 degree dip-slip source. Beach balls are used to show the radiation pattern of the moment tensor sources. (b) The recorded seismogram in trace 1. The red crosses show the P- and S-wave arrivals of event 1. The blue crosses show the P- and S-wave arrivals of event 2. (c) Separate wavefields of event 1 and 2.

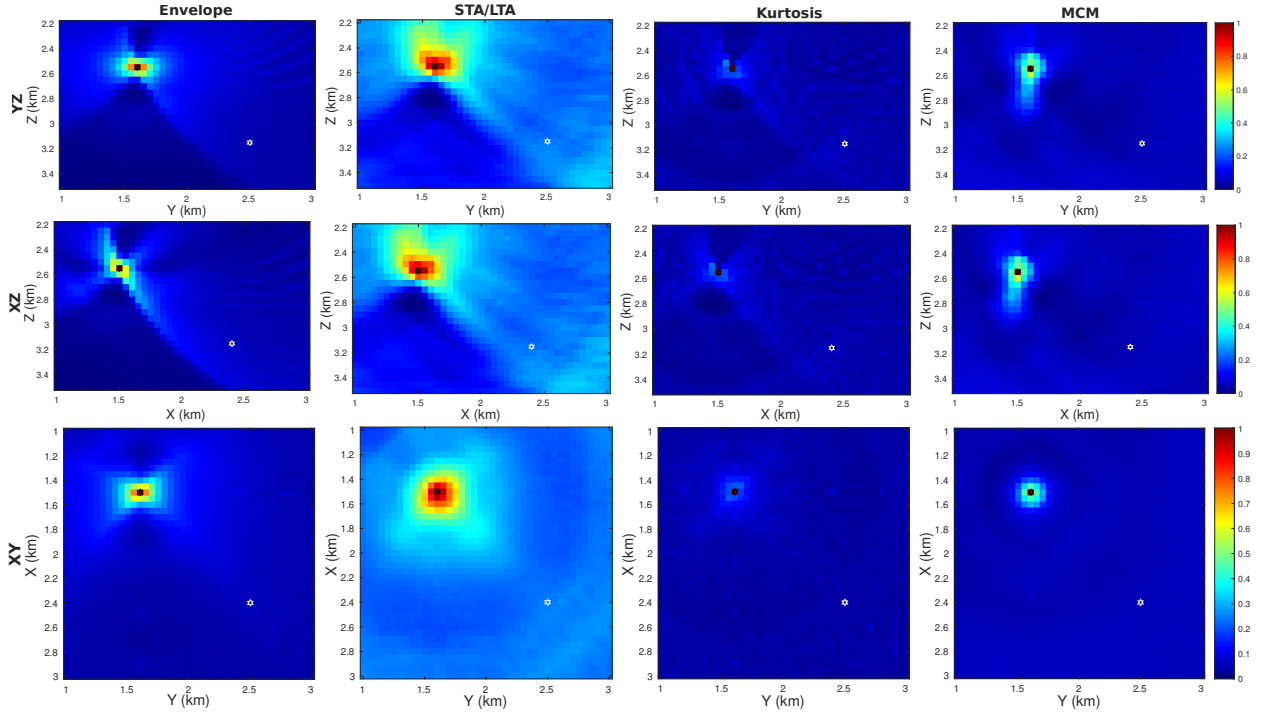


**Figure 15.** Profiles of the migration results through the true location of event 1 for the four migration methods. The slices are taken at the time of maximum stacking value for event 1. The stacking functions have been linearly normalized between 0 and 1. The black hexagon in the upper left part of the model represents the true location of event 1. Event 2 is also projected on the profile, shown as the white hexagon in the lower right part of the model. The first column shows results of envelope, second column for STA/LTA, third column for kurtosis, fourth column for MCM. The first row shows YZ (vertical) profiles, second row shows XZ (vertical) profiles, and third row shows XY (horizontal) profiles.

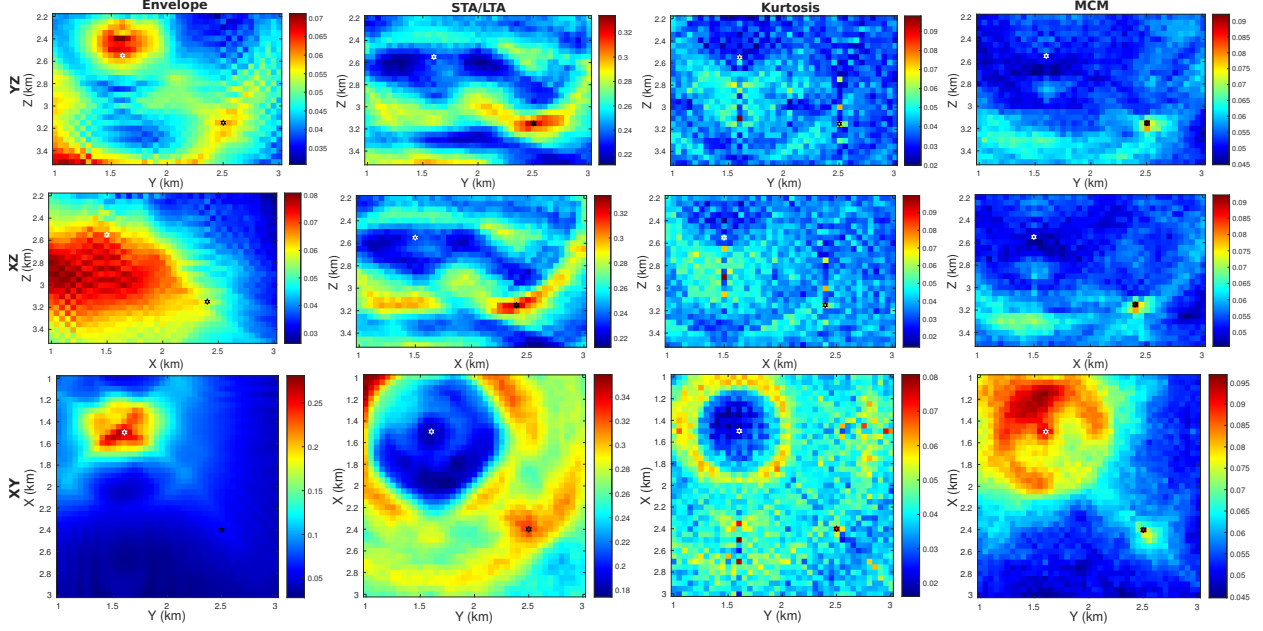


**Figure 16.** Profiles of the migration results through the true location of event 2 for the four migration methods. The slices are taken at the time of maximum stacking value for event 2. The black hexagon in the lower right part of the model represents the true location of event 2. Event 1 is also projected on the profile, shown as the white hexagon in the upper left. The first column shows results of Envelope, second column for STA/LTA, third column for kurtosis, fourth column for MCM. The first row shows YZ (vertical) profiles, second row shows XZ (vertical) profiles, third row shows XY (horizontal) profiles.

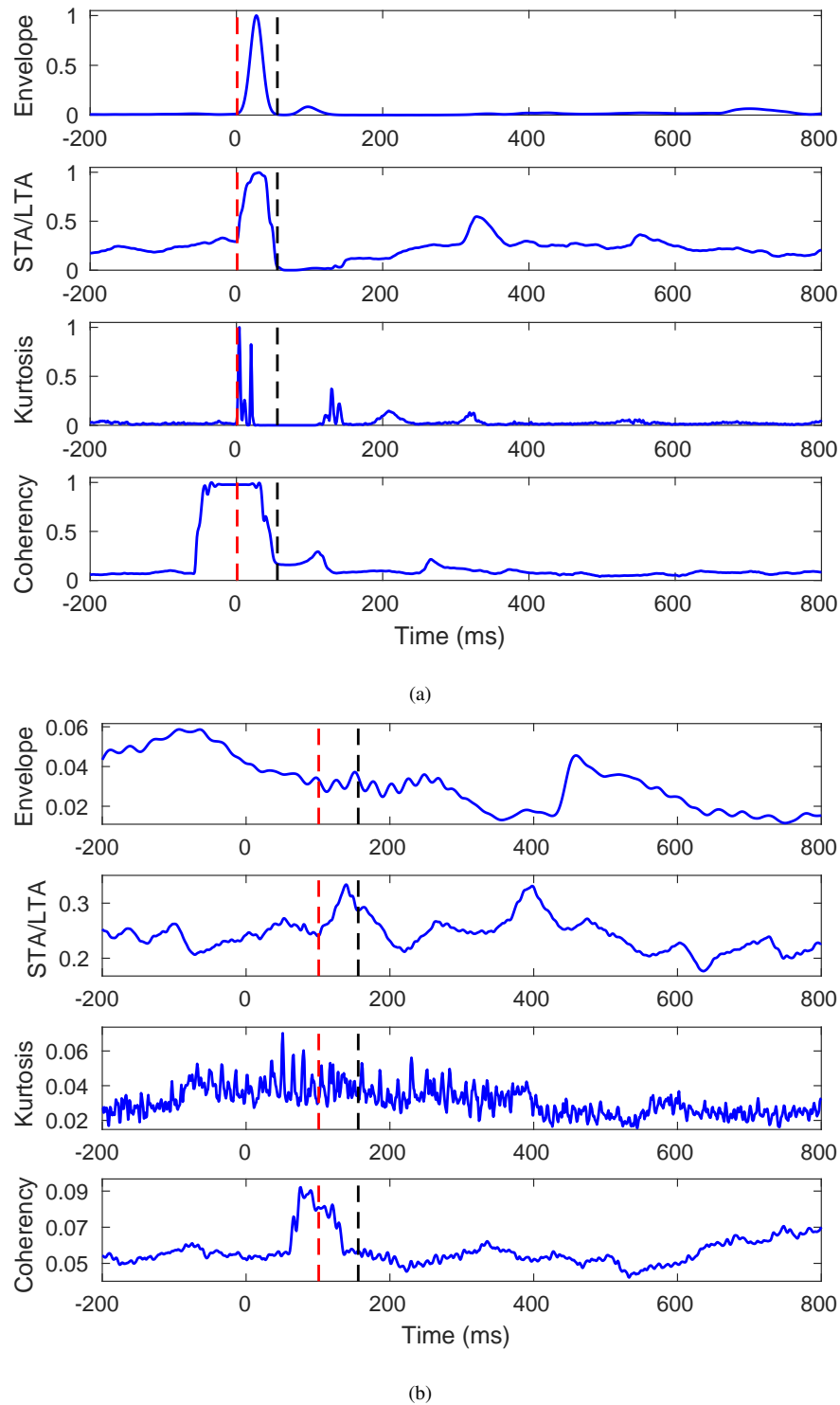


**Figure 17.** The stacking functions at the true source locations of (a) event 1 and (b) event 2 for the four methods. The red and black dashed line shows the origin time and end time of the event 1 and 2 respectively.

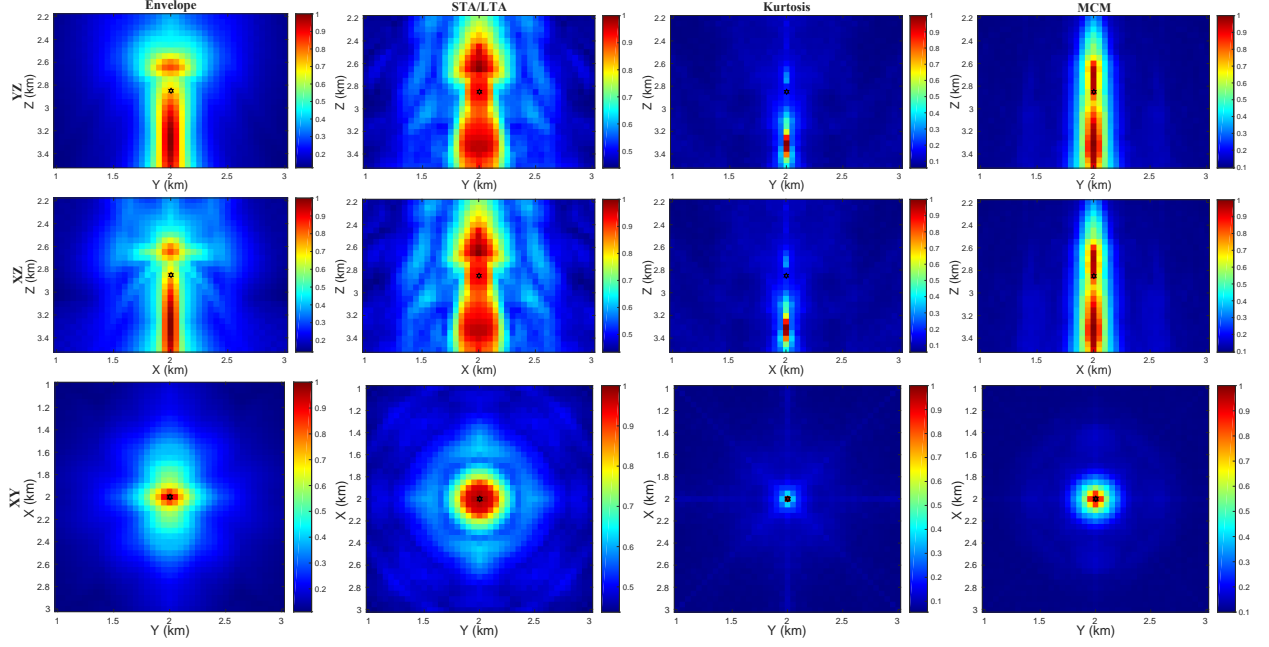


**Figure 18.** Profiles of the migration results using the low velocity model for the four methods. The profiles are obtained by projecting the maximum values along the time domain and the corresponding directions (i.e. for YZ profiles, projecting along the X direction; for XZ profiles, projecting along the Y direction; for XY profiles, projecting along the Z direction). The black hexagon in the middle of the figures represents the true source location. The first column shows results of envelope, second column for STA/LTA, third column for kurtosis, fourth column for MCM. The first row shows YZ (vertical) profiles, second row shows XZ (vertical) profiles, third row shows XY (horizontal) profiles.

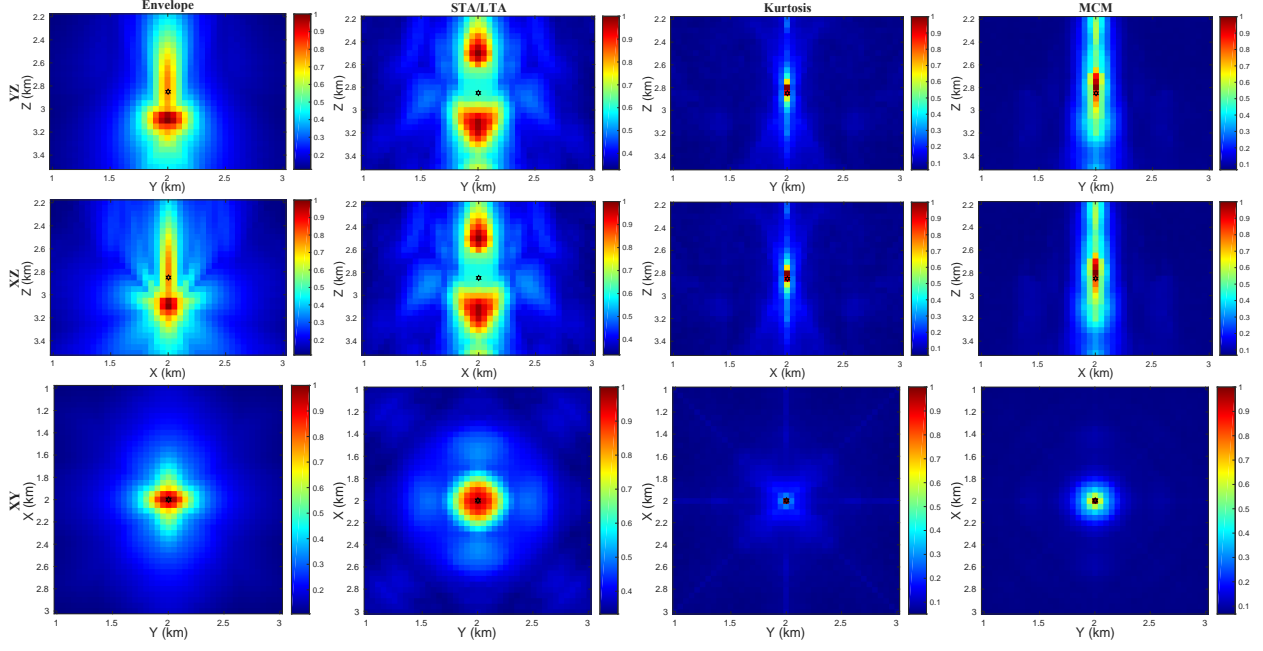


**Figure 19.** Profiles of the migration results using the high velocity model for the four methods. The profiles are obtained by projecting the maximum values along the time domain and the corresponding directions (i.e. for YZ profiles, projecting along the X direction; for XZ profiles, projecting along the Y direction; for XY profiles, projecting along the Z direction). The black hexagon in the middle of the figures represents the true source location. The first column shows results of envelope, second column for STA/LTA, third column for kurtosis, fourth column for MCM. The first row shows YZ (vertical) profiles, second row shows XZ (vertical) profiles, third row shows XY (horizontal) profiles.

**Table 2.** Location results of different methods and comparison with true source location using the low and high velocity models.

	Source location				Location error			
	X (km)	Y (km)	Z (km)	$T_0$ (s)	$\Delta X$ (m)	$\Delta Y$ (m)	$\Delta Z$ (m)	$\Delta T_0$ (s)
True	2.00	2.00	2.85	0.100	-	-	-	-
Low	Envelope	2.00	2.00	3.30	-0.056	0	0	450
	STA/LTA	2.00	2.00	2.65	0.105	0	0	200
	Kurtosis	2.00	2.00	3.30	-0.081	0	0	450
	Coherency	2.00	2.00	3.30	-0.135	0	0	450
High	Envelope	2.00	2.00	3.10	0.118	0	0	250
	STA/LTA	2.00	2.00	2.50	0.379	0	0	350
	Kurtosis	2.00	2.00	2.80	0.161	0	0	50
	Coherency	2.00	2.00	2.80	0.182	0	0	50

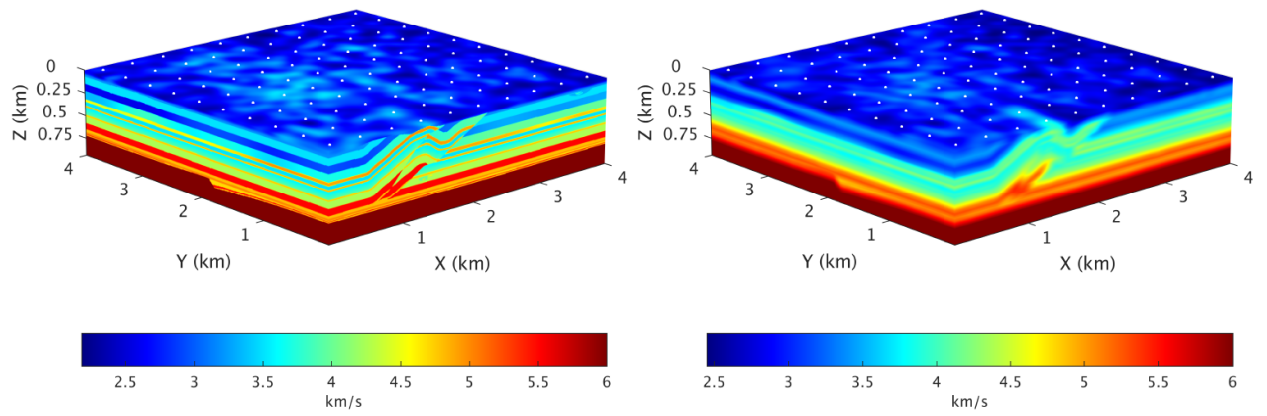


**Figure 20.** P-wave velocity model of the 3D overthrust model (Aminzadeh et al. 1997). White dots show the surface projection of the monitoring arrays. Left: original velocity model used for full wavefield modeling. Right: smoothed velocity model used for source location.

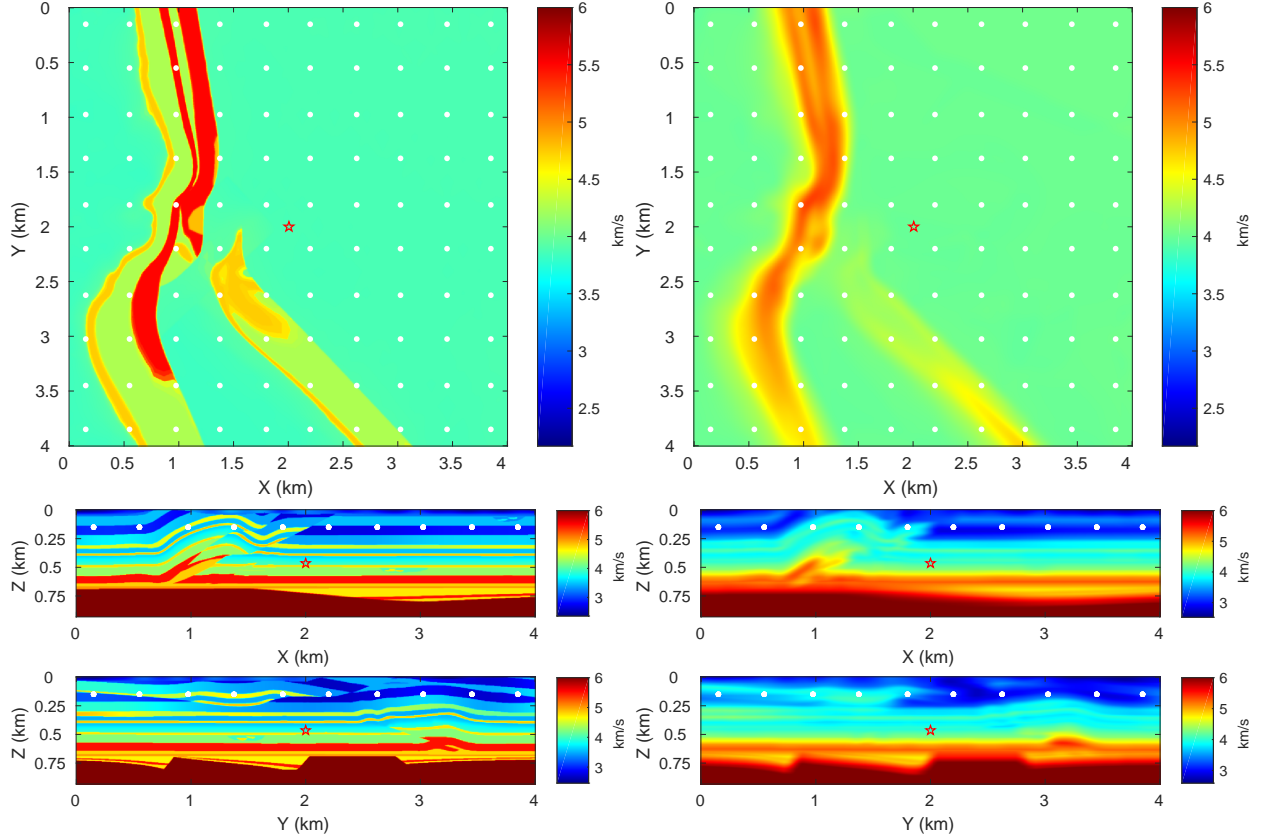


**Figure 21.** P-wave velocity profiles of the 3D overthrust model through the source point. Red star shows the location of the source and white dots show the projection of receivers. First row: horizontal profiles at the depth of 0.46 km. Second row: vertical profiles at 1.995 km in the Y direction. Third row: vertical profiles at 1.995 km in the X direction. Left: original velocity model used for full wavefield modeling. Right: smoothed velocity model used for source location.

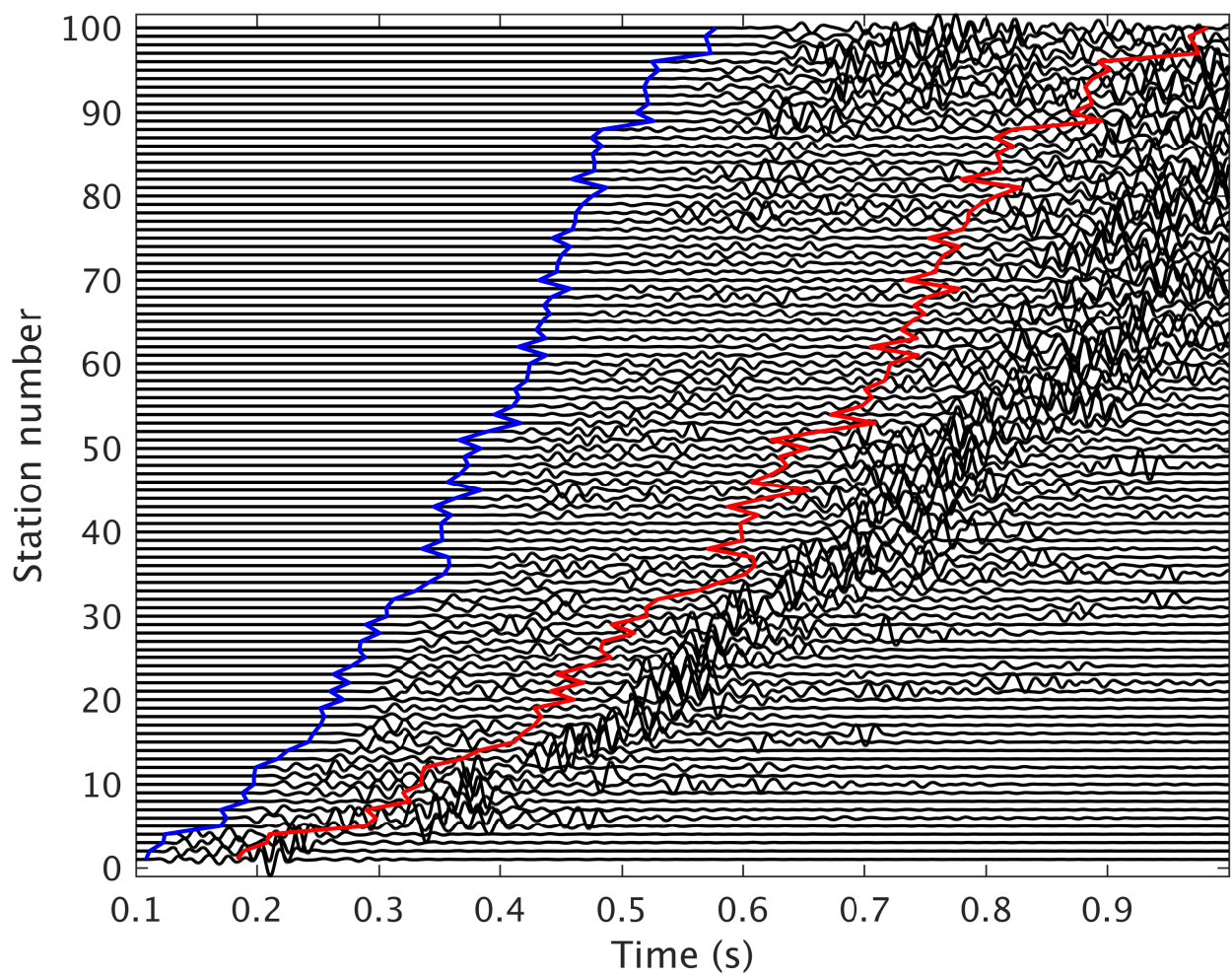


**Figure 22.** Record section of particle velocities in the Z direction for the 3D overthrust model. Blue line shows the calculated arrival times for the direct P-waves and red line shows the calculated arrival times for the direct S-waves. The recorded traces are numbered and aligned vertically according to horizontal offsets. Note that the calculated arrival times of the direct P- and S-waves are not smooth (zigzagged) because of strong 3D heterogeneity of the model.

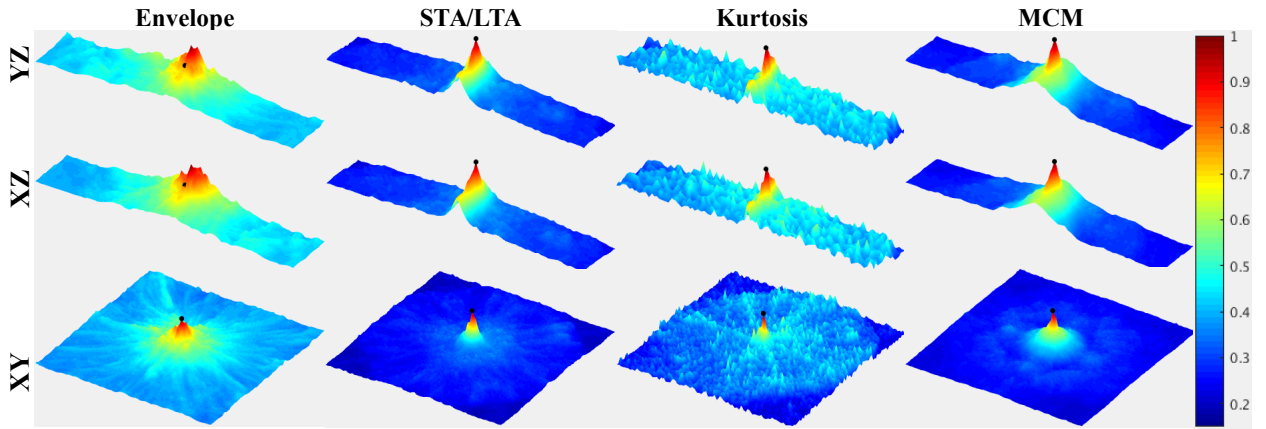


**Figure 23.** 3D profiles of the migration results using the smoothed overthrust velocity model for the four methods. The profiles are obtained by projecting the maximum stacking values along the time domain and the corresponding directions (i.e. for YZ profiles, projecting along the X direction; for XZ profiles, projecting along the Y direction; for XY profiles, projecting along the Z direction). Black balls show the true position of the source event. The migrated volumes of different methods are all linearly normalized to 0 - 1. The first column shows results of envelope, second column for STA/LTA, third column for kurtosis, fourth column for MCM. The first row shows YZ (vertical) 3D profiles, second row shows XZ (vertical) 3D profiles, third row shows XY (horizontal) 3D profiles.